Electronic Supplementary Information (ESI)

Asymmetric Orbital Hybridization at MXene-VO_{2-x} Interface Stabilizes Oxygen Vacancies for Enhanced Reversibility in Aqueous Zinc-ion Battery

Yuan Fang,‡[a] Chunhong Qi,‡[a] Weichao Bao,[b] Fangfang Xu,[b] Wei Sun,*[a] Bin Liu,[c] Xiqian Yu,[d] Lianjun Wang,[a] Wan Jiang,[a] Pengpeng Qiu*[a] and Wei Luo*[a]

[a] State Key Laboratory for Modification of Chemical Fibers and Polymer Materials, College of Materials Science and Engineering, Donghua University, Shanghai 201620, China. E-mail: weisun@dhu.edu.cn (Wei Sun); qiupengpeng@dhu.edu.cn (Pengpeng Qiu); wluo@dhu.edu.cn (Wei Luo)

[b] State Key Laboratory of High Performance Ceramics and Superfine Microstructure, Shanghai Institute of Ceramics, Shanghai 200050, China.

[c] School of Materials Science and Engineering, Shanghai University, Shanghai 200444, China.

[d] Beijing Advanced Innovation Center for Materials, Genome Engineering, Institute of Physics, Chinese Academy of Sciences, Beijing 100190, China.

‡ These authors contributed equally to this paper.

This file includes

Material and Methods

Figures S1 to S63

Tables S1 to S2

References

Material and Methods

Preparation of $Ti_3C_2T_x$ MXene nanosheets

The $Ti_3C_2T_x$ MXene nanosheets were obtained *via* the HCl/LiF assisted etching method. To be specific, 1.0 g of LiF was dispersed into 20 mL of HCl solution (9 M). The mixture was stirred for 10 min, followed by the addition of 1.0 g of Ti_3AlC_2 under magnetic stirring in ice bath. After stirring at 35 °C for 24 h, the obtained black solution was collected after centrifugation and washed with deionized water until the pH ≈ 6. The resulting sediment was dispersed into 250 mL of deionized water and then treated with ultrasound for 1 h under a nitrogen atmosphere. Then the supernatant was obtained by centrifugation at 3500 rpm for 30 min. Finally, the MXene solution is freeze-dried to obtain the MXene floccule.

Preparation of MXene-VO_2 sample

In a typical synthesis, 216 mg of $VO(acac)_2$ and 36 mg of $Ti_3C_2T_x$ MXene were dispersed in 60 mL THF and ultrasonicated for 20 min. Then, 4 mL of 30 % H_2O_2 was added into the solution above and stirred evenly for 2 h. Finally, the mixed solution was transferred to a 100 mL stainless Teflon-lined autoclave and kept at 130 °C for 3 h. After cooling to room temperature, the product was collected by centrifuge and washed repeatedly by deionized water and ethanol. The dark grey MXene-VO_2 powder was obtained after lyophilization.

Preparation of MXene-VO_{2-x} sample

The MXene-VO_2 was annealed in muffle furnace at 350 °C for 2 h to obtain the MXene-V_2O_5. Then 200 mg of MXene-V_2O_5 was dispersed in a 12.5 mL mixed solution of water and ethylene glycol (2:3 by volume) under magnetic stirring. After that, the solution was transferred to a 25 mL Teflon-lined sealed autoclave at 200 °C for 6 h. When the autoclave cooled down, the MXene-VO_{2-x} was washed repeatedly with deionized water and ethanol and required a vacuum freezing drying process.

Preparation of MXene/VO_2 sample

Firstly, the VO_2 was synthesized by the same method for preparing MXene-VO_2 without the addition of MXene. Then the VO_2 and MXene were mixed with the weight mass ratio of 1.18:1 (determined by ICP-OES) following the grinding process to get uniformly distributed powder.

Preparation of MXene/VO_{2-x} sample

The VO_{2-x} was prepared through the same oxidation-reduction phase transition process using VO_2. Then the VO_{2-x} and MXene were mixed with the weight mass ratio of 1.22:1 (determined by ICP-OES) following the grinding process to get uniformly distributed powder.

Preparation of GO-VO_2, SiO_2-VO_2, CNT-VO_2 and CF-VO_2

These heterojunctions with VO_2 deposited onto the different substrates were

produced by the same synthetic method of preparing MXene-VO_2, except that the equal GO, SiO_2, CNT and CF were used to take place of MXene.

Preparation of MXene-ZnO heterojunction

54 mg of $Zn(acac)_2$ and 9 mg of $Ti_3C_2T_x$ MXene were dispersed in 15 mL THF and ultrasonicated for 20 min. Then, 0.9 mL of 30 % H_2O_2 was added into the solution above and stirred evenly for 2 h. Finally, the mixed solution was transferred to a 25 mL stainless Teflon-lined autoclave and kept at 130 °C for 3 h. After cooling to room temperature, the product was collected by centrifuge and washed repeatedly by deionized water and ethanol. The white MXene-ZnO powder was obtained after lyophilization.

Preparation of MXene-MoO_2 heterojunction

72 mg of $MoO_2(acac)_2$ and 9 mg of $Ti_3C_2T_x$ MXene were dispersed in 15 mL THF and ultrasonicated for 20 min. Then, 1.5 mL of 30 % H_2O_2 was added into the solution above and stirred evenly for 2 h. The subsequent solvothermal process is the same with the synthesis MXene-ZnO.

Characterizations

The morphology of the cathode materials was observed using SEM (TESCAN/MAIA3, Czech), TEM (JEOL JEM-2100F), and a Cs-corrected TEM (Themis ETEM, Thermo Fisher Scientific). SAED and elemental mapping were

performed during the TEM measurement. ICP-OES (Prodigy-ICP) was used to ascertain the proportion of metal. AFM was conducted with a Dimension FastScan/Icon atomic force microscope with tapping mode. XRD patterns were collected by Bruker D4 diffractometer with Ni-filtered Cu Kα beam at 40.0 kV and 40 mA. XPS was tested by Escalab 250xi X-ray photoelectron spectrometer. All the binding energies were modified using the C 1s standard peak at 284.8 eV. Synchrotron XPS measurements were performed at the BL02B beamline in Shanghai Synchrotron Radiation Facility (SSRF). EPR data were recorded at room temperature using a Bruker JEOL JES-FA200 spectrometer. XAFS measurements at V K-edge in transmission mode were performed at the BL14W1 in SSRF. The incident photon beam was selected by a double-crystal Si (111) monochromator after a collimating mirror and focused by a toroidal mirror. The FTIR is taken by using the Fourier transform infrared spectrometer (Nicolet iS50). The soft X-ray absorption spectroscopy (sXAS) measurements were carried out in total electron yield (TEY) mode at the BL02B beamline in SSRF. Zeta potential was measured using the Andon paar Litersizer500.

Electrochemical measurements

The CR2025-type coin cells were utilized to evaluate the electrochemical performance of MXene-VO_{2-x} as the active material. Firstly, uniform slurries were prepared by grinding the active material, conductive carbon, and polyvinylidene fluoride (PVDF) with a weight ratio of 7:2:1. Next, the cathodes were fabricated by putting the slurry onto Ti foils (d = 12 mm) and subsequently vacuum drying under 60 ℃

overnight. The coin-type cells were assembled using Zn anode, 3M $Zn(CF_3SO_3)_2$ (98 %, Aladdin) aqueous electrolyte, glass microfiber filter (0.68 mm thickness, Whatman, GF/D) separator and cathode electrode in air. Battery performance was measured using a LAND battery testing system. The specific capacity was calculated based on the mass of active materials. Additionally, CHI760e electrochemical workstation was performed to obtain CV curves and EIS.

Computational methods

All theoretical calculations were conducted within the framework of DFT using the Vienna Ab-initio Simulation Package (VASP),[1] using the Perdew-Burke-Ernzerhof (PBE) formulation in the generalized gradient approximation (GGA) for first-principles calculations. The interaction between electrons and ions was described by projected augmented wave (PAW) pseudopotentials.[2,3] All calculations were used the cutoff energy of 450 eV for the plane wave basis, and the convergence criteria for ion relaxation and electron self-consistent calculations were set to 0.05 eV $Å^{-1}$ and 10^{-4} eV, respectively. The Brillouin zone was sampled using a Monkhorst-Pack 2 × 2 × 1 k-point grid. A vacuum layer of 15 Å was inserted in the Z direction for surface isolation, thereby avoiding the interaction between two adjacent surfaces. The Grimme's DFT-D3 correction method[4] was utilized to incorporate van der Waals interactions into the calculations. Additionally, the dipole correction along the surface normal was taken into account.

The adsorption properties of different samples for Zn^{2+} and V^{4+} ions were evaluated

by comparing the adsorption energy, which is defined as:

$$E_{ads} = E_{absorb/surf} - E_{surf} - E_{absorb}$$

where $E_{absorb/surf}$, E_{surf} and E_{absorb} represent the total energies of the substrate with adsorbate (s), the clean substrate, and the isolated adsorbate, respectively. The climbing image nudged elastic band (CI-NEB) approach[5] was employed to accurately determine the diffusion energy barrier and thoroughly analyze the diffusion behaviors of Zn^{2+} on distinct structures. The trajectory from reactants to products was divided into eight structural images, and the intermediate images were iteratively optimized until the vertical force converged to a value below 0.05 eV $Å^{-1}$.

The formation energy of oxygen vacancies was calculated by the following formula:

$$E_f = E_{all\_O} - E_{all} + \frac{1}{2}E_{O_2}$$

where E_f is the formation energy of oxygen vacancies, E_{all_O} is the energy with the oxygen vacancy, E_{all} is the energy without the oxygen vacancy, E_{O_2} is the energy of O_2 molecule. The migration energy barrier of oxygen vacancies in the structures were also calculated by CI-NEB.

The molecular dynamic (MD) calculations are implemented using the Large-scale Atomic-Molecular Massively Parallel Simulator (LAMMPS) software package.[6] The classic molecular dynamics (MD) simulations were performed to explore the decomposition behaviors of GeH monolayer sheets subjected to a variety of environmental conditions from nanoscale level. Here, MD box with dimensions of approximately 27 × 25 × 120 $Å^3$ was created, in which one free-standing $Ti_3C_2O_2$ MXene monolayer sheet composed of 240 Ti, 160 C and 160 O atoms was placed in

the center of the MD box. For the decomposition study of GeH monolayer sheet, three circumambient environment conditions including 200 O_2, 100 H_2O+100 O_2 and 200 H_2O_2 molecules in the MD box were taken into consideration for comparison. Periodic boundary conditions (PBCs) were imposed on all directions. Prior to conducting MD simulations, as-generated MXene-based systems were quasi-statically relaxed to a local minimum-energy configuration via conjugate gradient method within the tolerances of energy and force of 1.0×10^{-4} Kcal/mol and 1.0×10^{-4} Kcal/(mol·Å), respectively. Subsequently, the as-minimized systems were equilibrated at conditions of 1000 K and confining pressure of 1 atm for 100,000 timesteps under NPT ensemble (constant number of particles, constant pressure, and constant temperature, in which the pressure was controlled at the two planar directions of MXene. Finally, MD production of 2,000,000 (5,000,000) timesteps on the as-equilibrated systems were performed at target temperature (1000 K) under NVT ensemble for examining the decomposition behaviors. During the MD simulations, the temperature and pressure were controlled by Nosé–Hoover thermostat and Nosé–Hoover barostat methods with damping time of 100 and 1000 timesteps, respectively. The velocity-Verlet integration algorithm with a timestep of 0.1 fs was utilized to integrate the Newton's motions in the MD calculations. To describe the atomic interactions in the MXene-based system, the first-principles-based ReaxFF potential[7] was employed. Because it is composed of three potential terms including bond-order-dependent covalent interaction, nonbonded standard Coulomb and Morse interaction terms, the ReaxFF forcefield is able to mimic chemical reactions such as dissociation and formation of covalent bonds. Moreover, previous studies show

that the ReaxFF potential predict the structural properties and chemical behaviors of various nanostructural systems subjected to various conditions such as heating and straining[8-11].

Supporting Figures

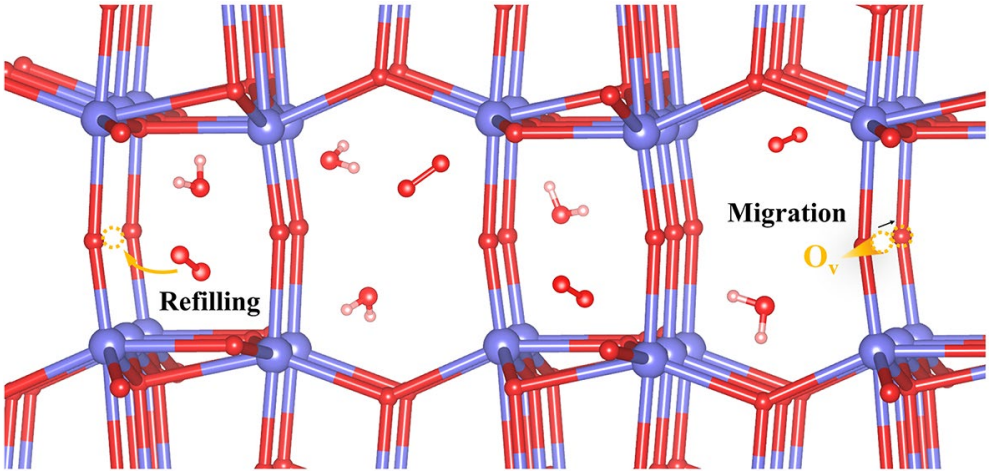

Fig. S1. Schematic illustration for the change of O_v during electrochemical redox reactions. O_v tend to migrate and be refilled in the VO_2 crystal framework.

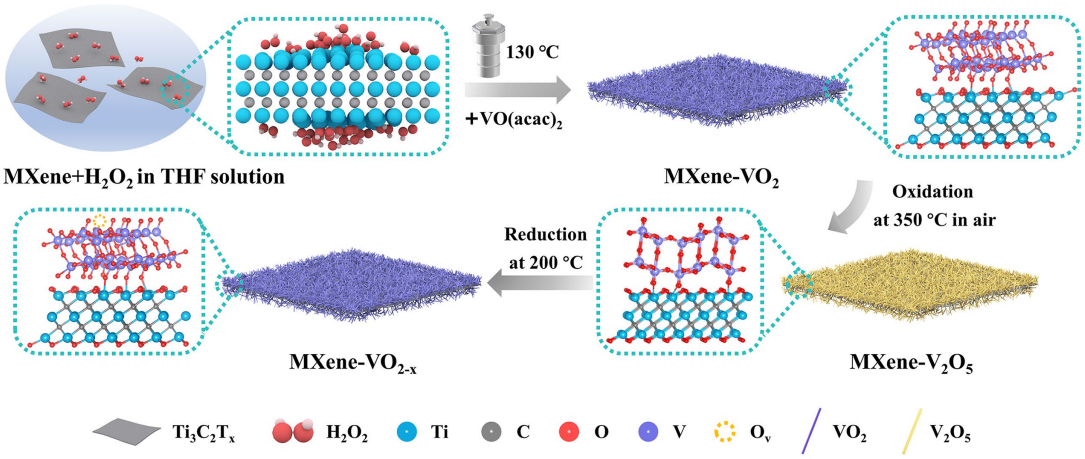

Fig. S2. Schematic illustration of the synthesis of covalent MXene-VO_{2-x} heterostructure.

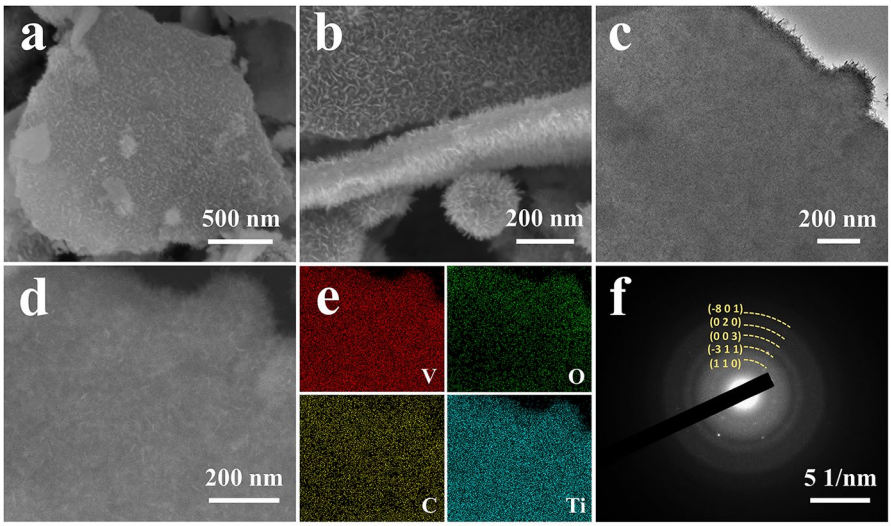

Fig. S3. The morphology characterization of MXene-VO_2. (a, b) SEM images. (c) Low-magnification TEM image. (d, e) HAADF-STEM image and the corresponding EDX maps of V, O, C, and Ti. (f) The corresponding SAED pattern of the basal plane of VO_2 (B).

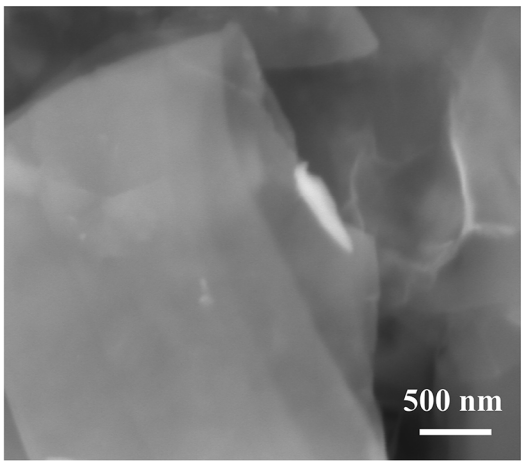

Fig. S4. SEM image of MXene nanosheets.

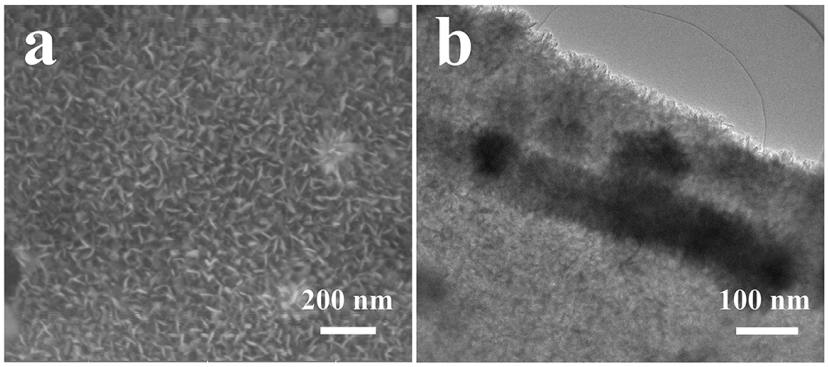

Fig. S5. The morphology characterization of MXene-VO_{2-x}. (a) SEM image. (b) Low-magnification TEM image.

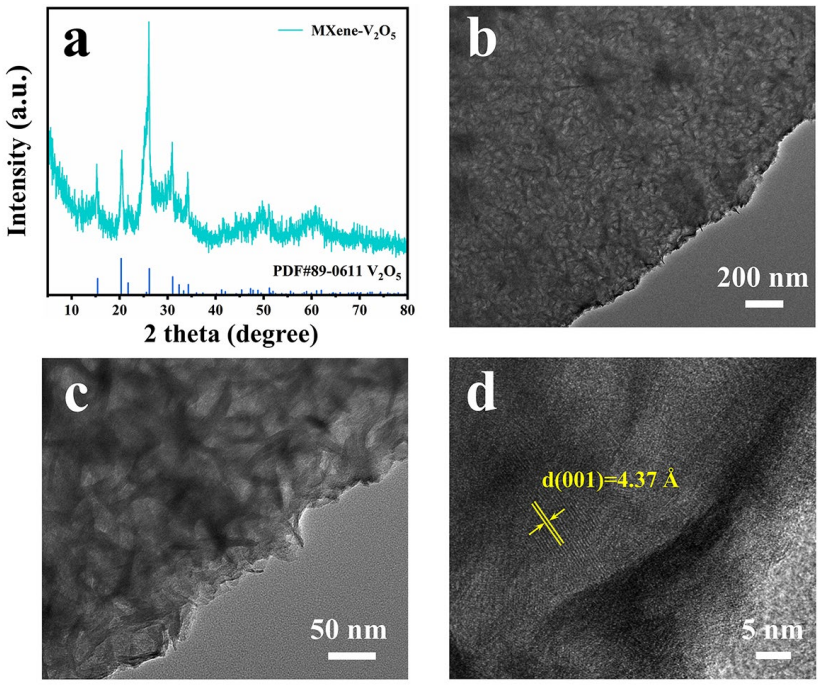

Fig. S6. The phase and morphology characterization of the MXene-V_2O_5. (a) XRD pattern of MXene-V_2O_5. The diffraction peaks of MXene-V_2O_5 match well with the standard orthorhombic V_2O_5 (JCPDS NO. 89-0611), indicating the complete phase transition. (b, c) Low-magnification TEM images, showing the unchanged morphology of MXene-V_2O_5. (d) High resolution TEM image. The lattice spacing of 4.37 Å is assigned to the (001) crystal plane of orthorhombic V_2O_5, further demonstrating the successful transformation.

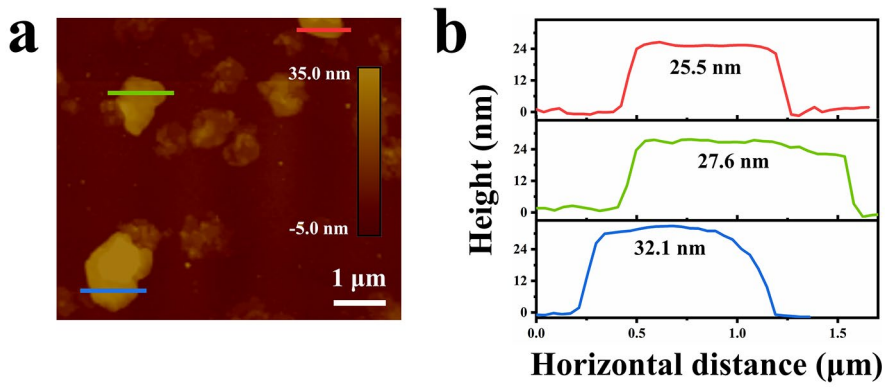

Fig. S7. Thickness measurement of MXene-VO_{2-x}. (a) AFM image of MXene-VO_{2-x}. (b) Three typical height curves of the 2D nanosheets.

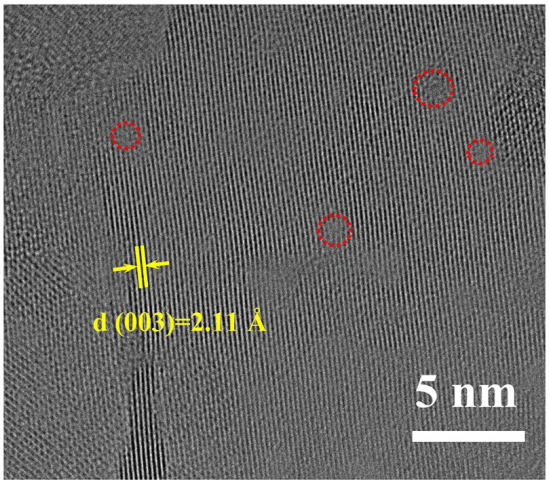

Fig. S8. Atom-resolved HAADF-STEM image of MXene-VO_{2-x}. The lattice disorders were labelled by red circles.

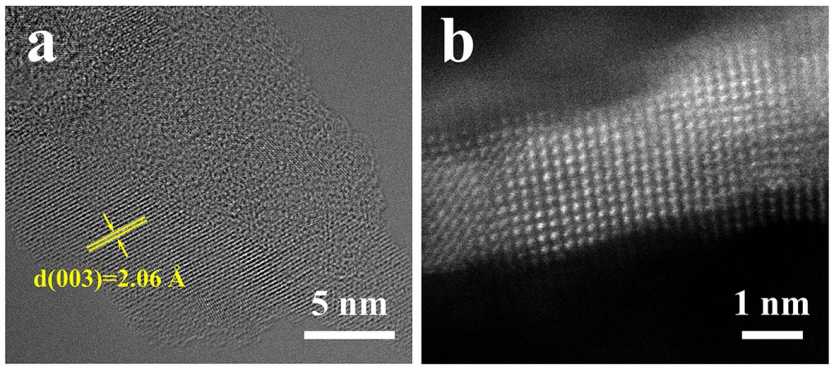

Fig. S9. Atom-resolved HAADF-STEM images of MXene-VO_2. The observed smaller lattice spacing of 2.06 Å corresponds to the (003) crystal plane of VO_2 (B).

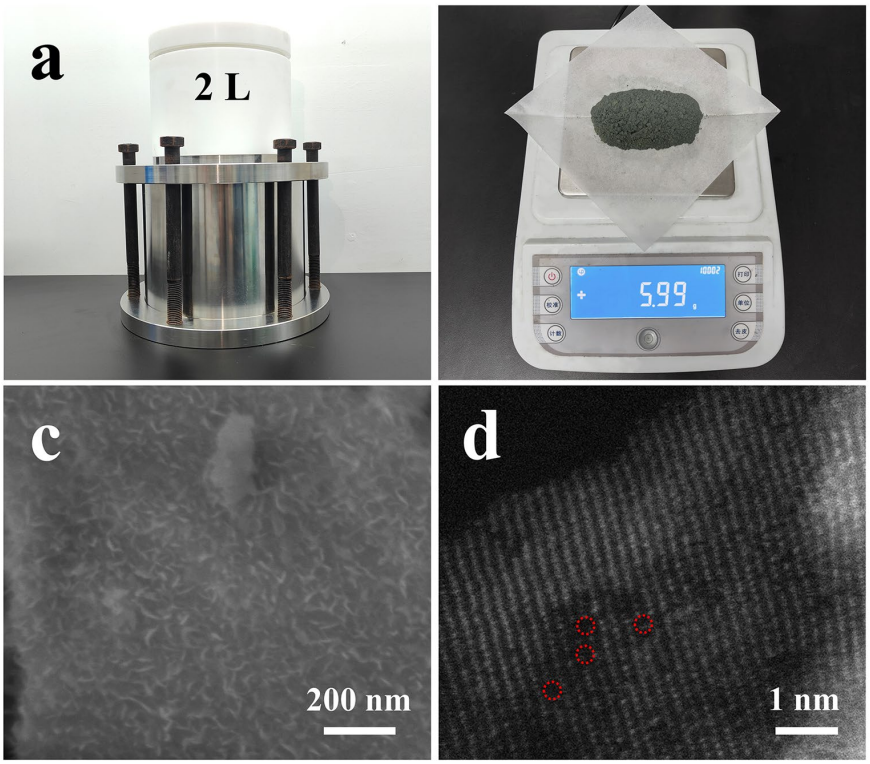

Fig. S10. Synthesis of MXene-VO_{2-x} covalent heterostructure by using a 2L autoclave. (a) Digital photograph of the 2 L Teflon-lined sealed autoclave. (b) Digital photograph of the MXene-VO_{2-x} powder produced using the scaled-up procedure. Corresponding (c) SEM and (d) atom-resolved HAADF-STEM images.

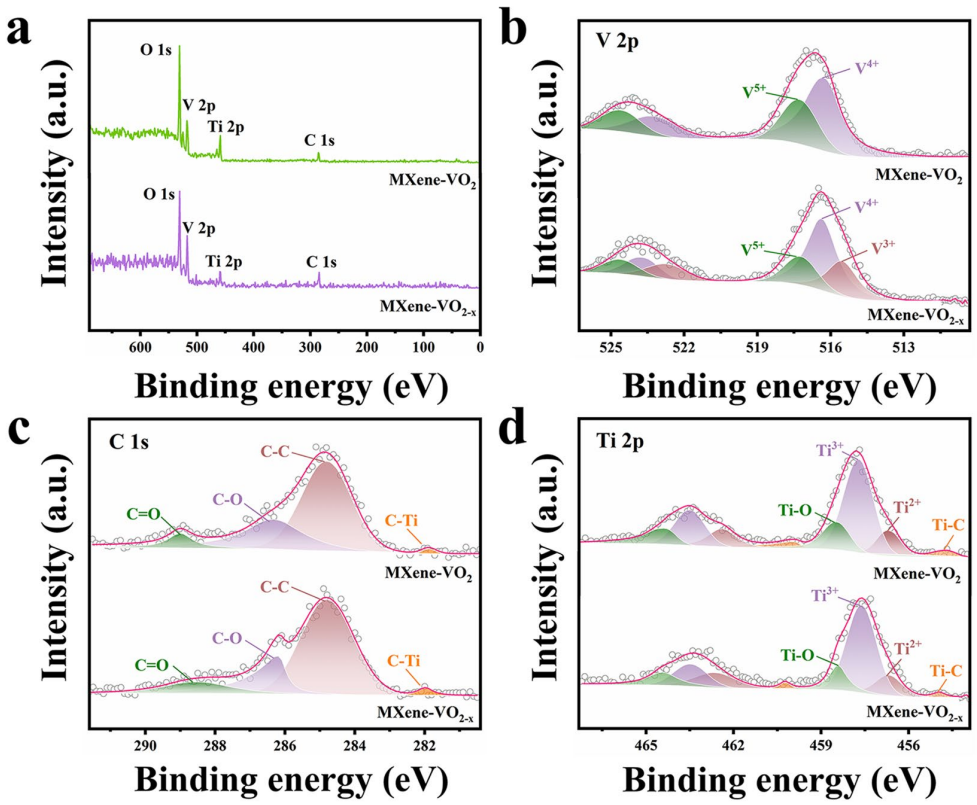

Fig. S11. XPS spectra of MXene-VO_2 and MXene-VO_{2-x}. (a) Full spectra. (b) V 2p spectra. (c) C 1s spectra and (d) Ti 2p spectra.

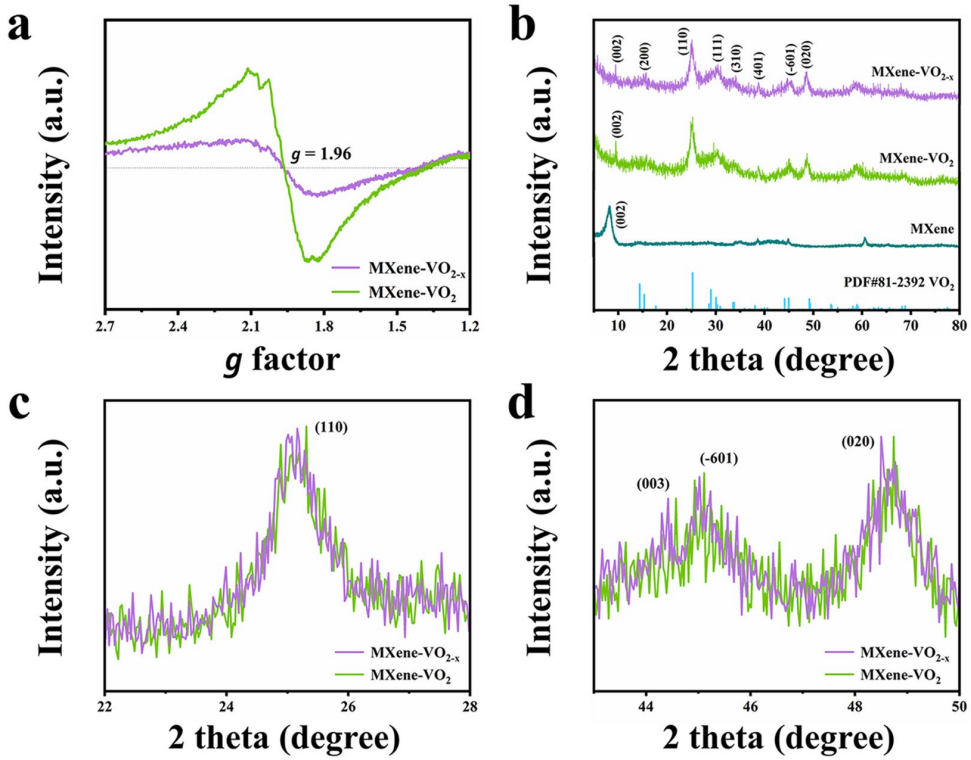

Fig. S12. The presence of O_v can be confirmed through EPR and XRD measurements. (a) EPR spectra of MXene-VO_{2-x} and MXene-VO_2. (b) XRD patterns of MXene-VO_{2-x} and MXene-VO_2. (c, d) Magnified views of the (110), (003), (-601), and (020) diffraction peaks of MXene-VO_{2-x} and MXene-VO_2.

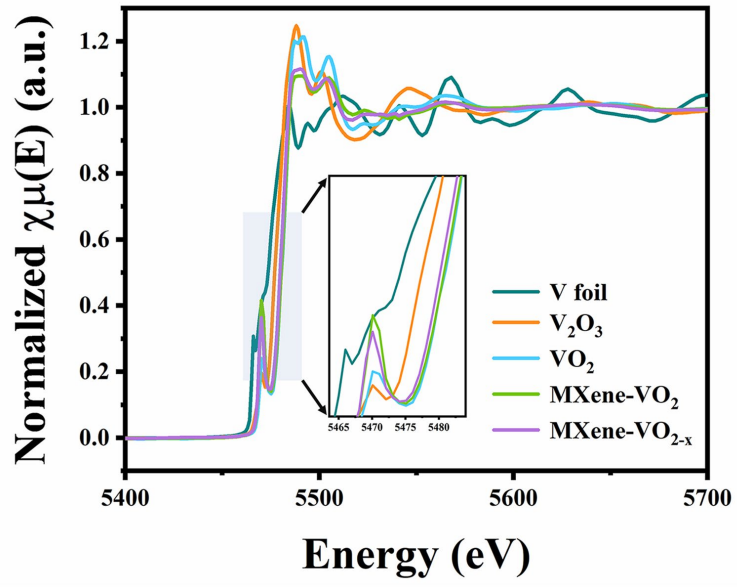

Fig. S13. Normalized XANES spectra of V K-edge for V foil, V_2O_3, VO_2 (B), MXene-VO_2 and MXene-VO_{2-x}.

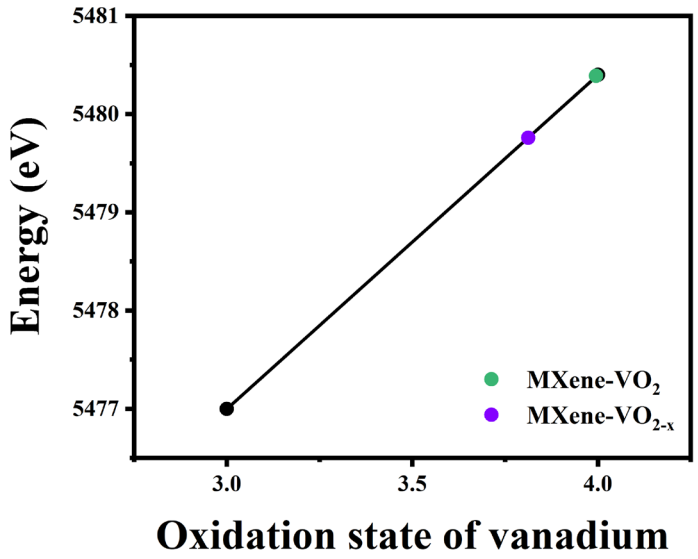

Fig. S14. The oxidation state fitting of V element in the MXene-VO_2 and MXene-VO_{2-x} by using the edge-jump energies (at 50 % level) of standard samples.

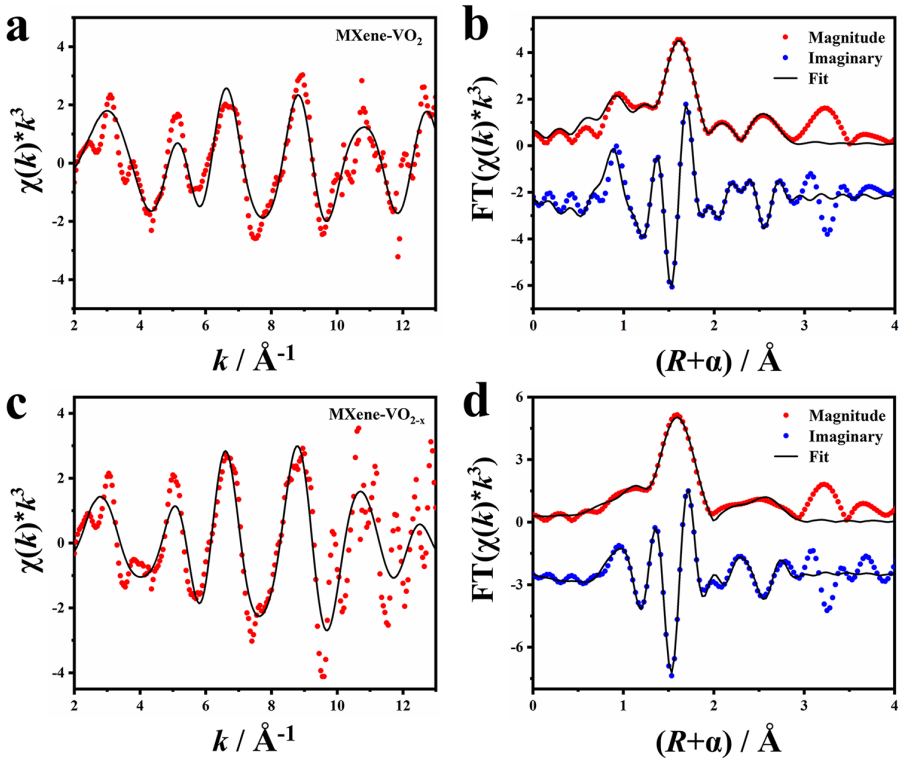

Fig. S15. Fitting results for V K-edge EXAFS of MXene-VO_2 and MXene-VO_{2-x}. V K-edge EXAFS (points) and the curvefit (line) for (a) MXene-VO_2 and (c) MXene-VO_{2-x}, shown in k^3 weighted k-space. V K-edge EXAFS (points) and curvefit (line) for (b) MXene-VO_2 and (d) MXene-VO_{2-x}, shown in R-space (FT magnitude and imaginary component). The data are k^3 weighted and not phase-corrected.

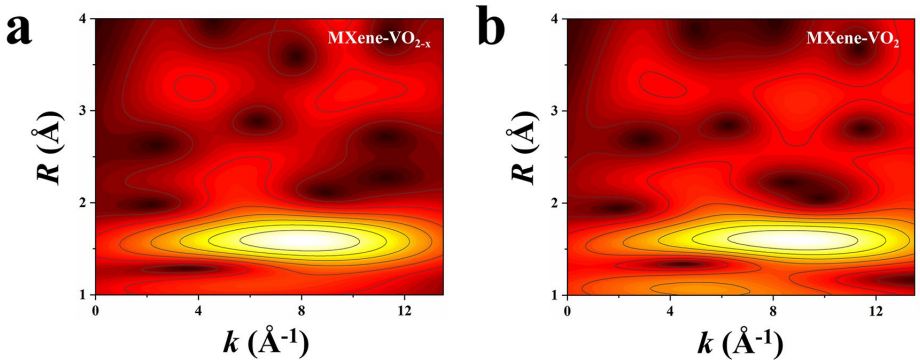

Fig. S16. WT-EXAFS plots are performed to provide more information in both *R* and *k* spaces. (a) MXene-VO_{2-x}. (b) MXene-VO_2.

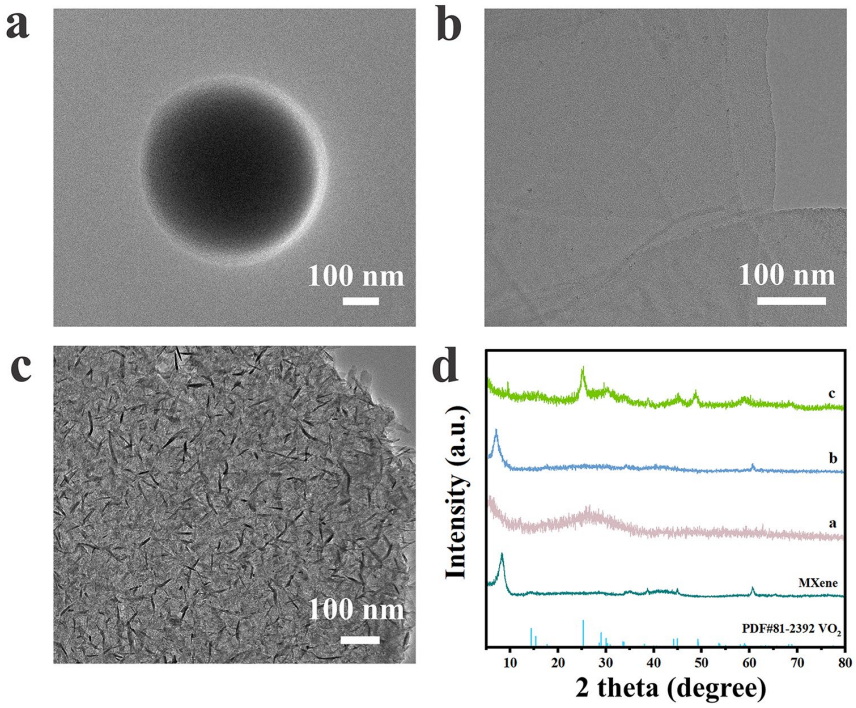

Fig. S17. TEM images of the contrast samples synthesized by adjusting the addition of MXene and H_2O_2. (a) The sample made only from THF solvent and $VO(acac)_2$. (b) The sample prepared with the presence of MXene. (c) The MXene-VO_2 sample synthesized with the introduction of both $Ti_3C_2T_x$ MXene and H_2O_2. (d) Corresponding XRD patterns.

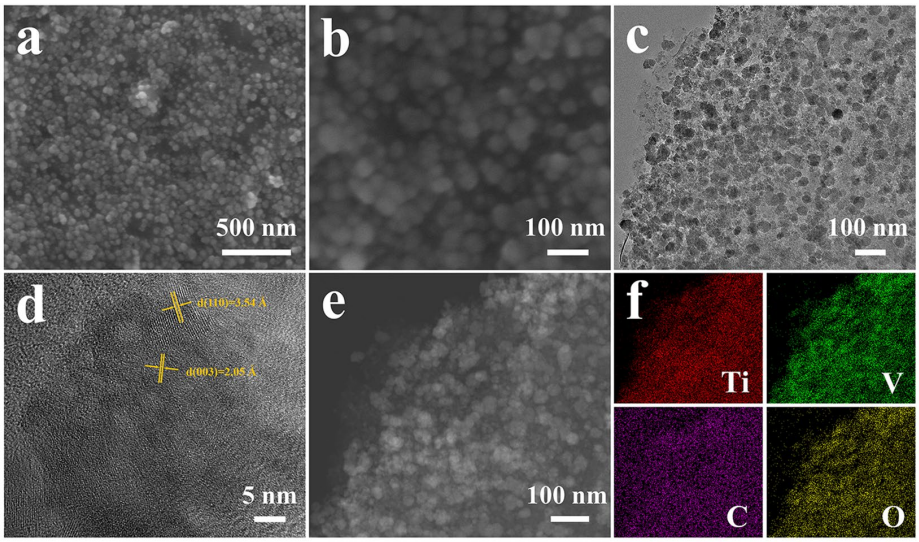

Fig. S18. The morphology characterization of the sample made by pure H_2O rather than H_2O_2. (a, b) SEM images. (c, d) Low-magnification and high resolution TEM images. (e, f) HAADF-STEM image and the corresponding EDX maps of Ti, V, C, and O.

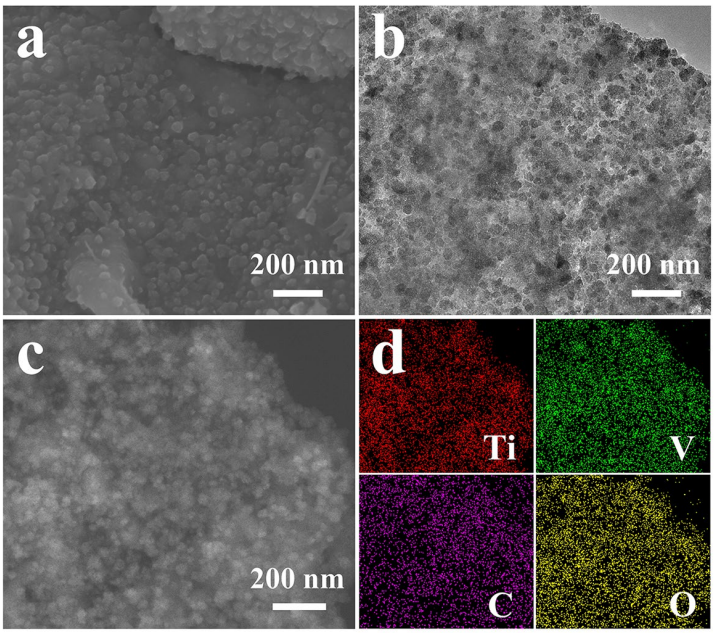

Fig. S19. The morphology characterization of the O_v-incorporated sample made by H_2O. (a) SEM image. (b) Low-magnification TEM image. (c, d) HAADF-STEM image and the corresponding EDX maps of Ti, V, C, and O. It is evident that the distribution of Ti element is uneven.

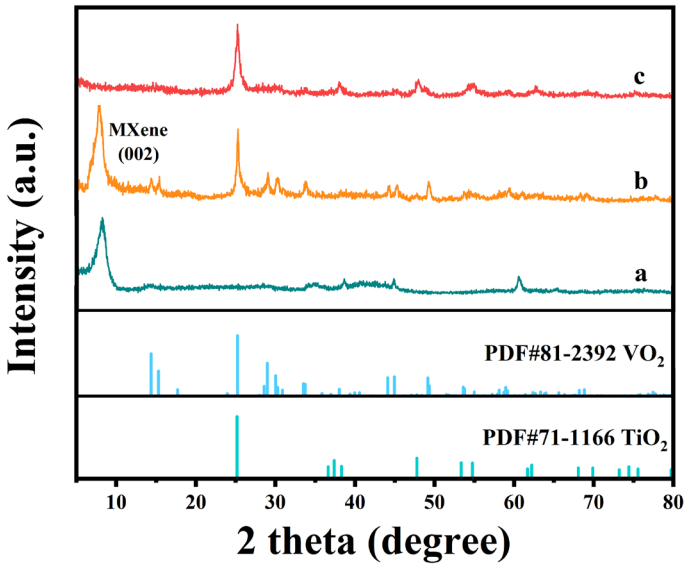

Fig. S20. XRD patterns. (a) MXene. (b) The sample made by pure H_2O. (c) The O_v-incorporated sample made by pure H_2O. The peak of MXene in sample C vanished completely with the formation of TiO_2.

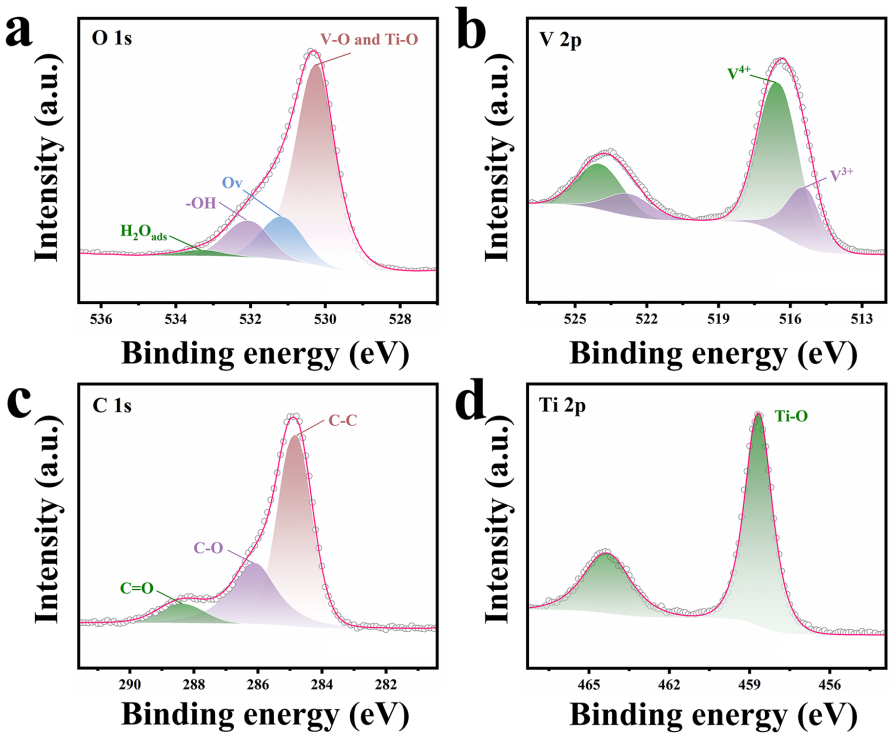

Fig. S21. XPS spectra of the O_v-incorporated sample made by pure H_2O. (a) O 1s spectrum without the formation of Ti-O-V covalent bond. (b) V 2p spectrum. The small characteristic peak of V^{3+} originates from the introduction of O_v. (c) C 1s spectrum without the signal of C-Ti. (d) Ti 2p spectrum only with the characteristic peak of Ti-O.

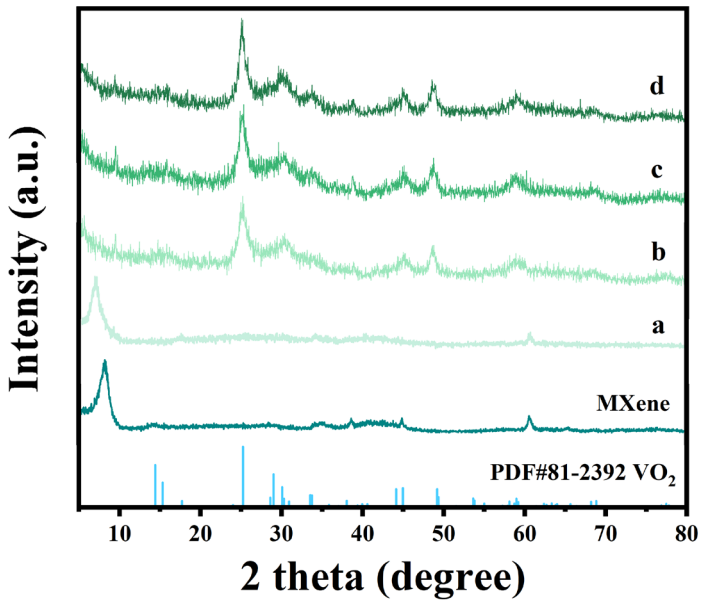

Fig. S22. XRD patterns of contrast samples synthesized by regulating the volume of H_2O_2. (a) 0 vol % H_2O_2. (b) 3.2 vol % H_2O_2. (c) 6.3 vol % H_2O_2. (d) 9.1 vol % H_2O_2.

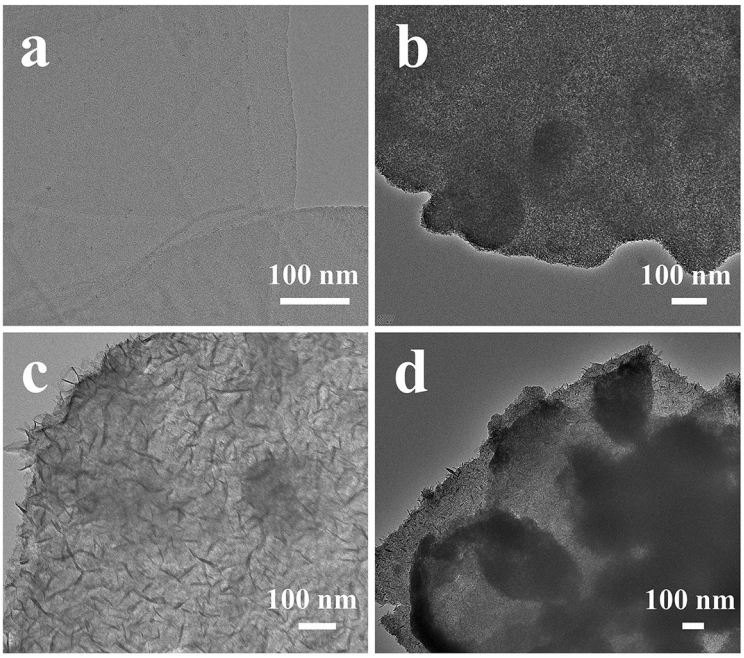

Fig. S23. Corresponding TEM images. (a) 0 vol % H_2O_2. (b) 3.2 vol % H_2O_2. (c) 6.3 vol % H_2O_2. (d) 9.1 vol % H_2O_2.

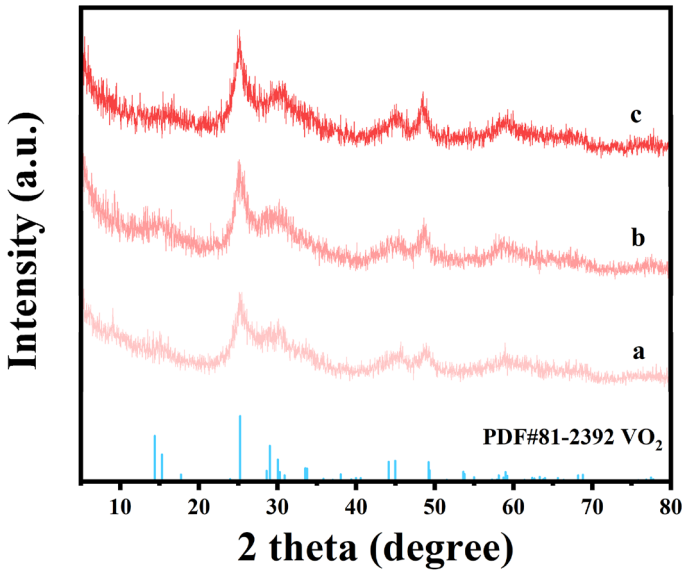

Fig. S24. XRD patterns of contrast samples prepared by controlling the hydrothermal reaction time. (a) 1 h. (b) 3 h. (c) 6 h. The peak intensity of VO_2 is gradually enhanced as the increase of VO_2 thickness.

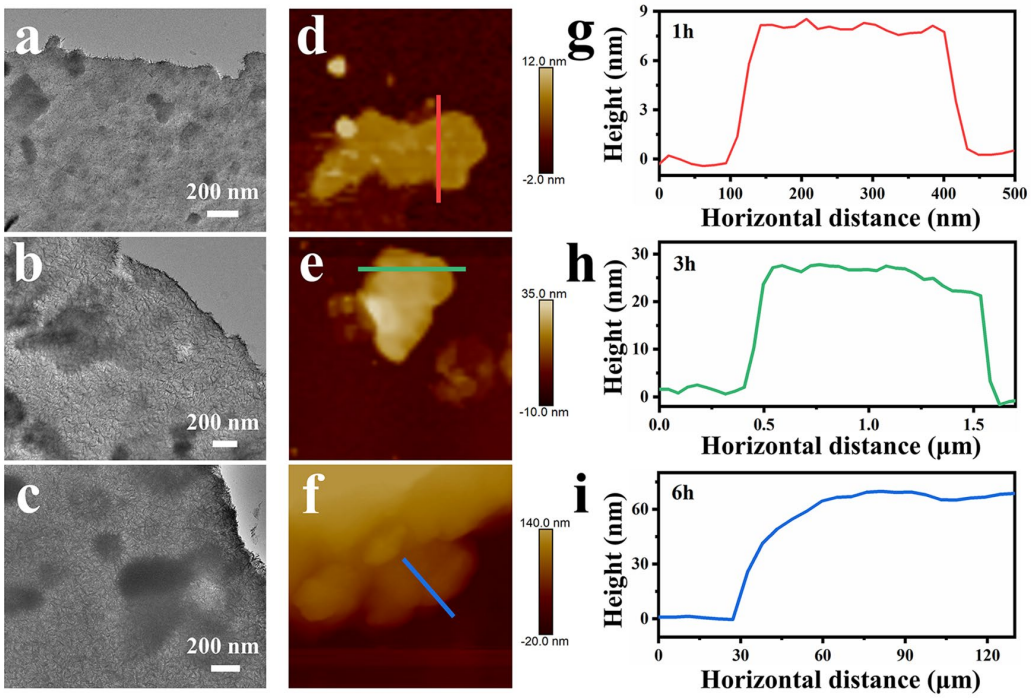

Fig. S25. Morphology characterization of contrast samples under different hydrothermal reaction time. TEM images of samples made through (a) 1 h, (b) 3 h, and (c) 6 h. AFM images and corresponding height curves of 2D nanosheets made through (d, g) 1 h, (e, h) 3 h, and (f, i) 6 h.

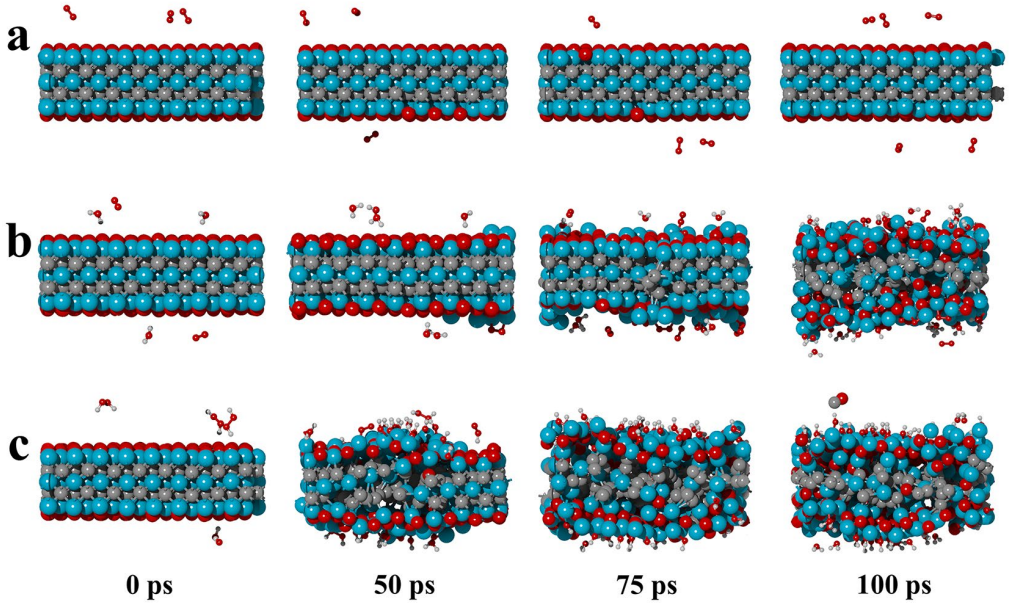

Fig. S26. The change of MXene structure after 0, 50, 75 and 100 ps oxidation at 1000 K under three environments. (a) O_2 molecules. (b) O_2 and H_2O molecules. (c) H_2O_2 molecules.

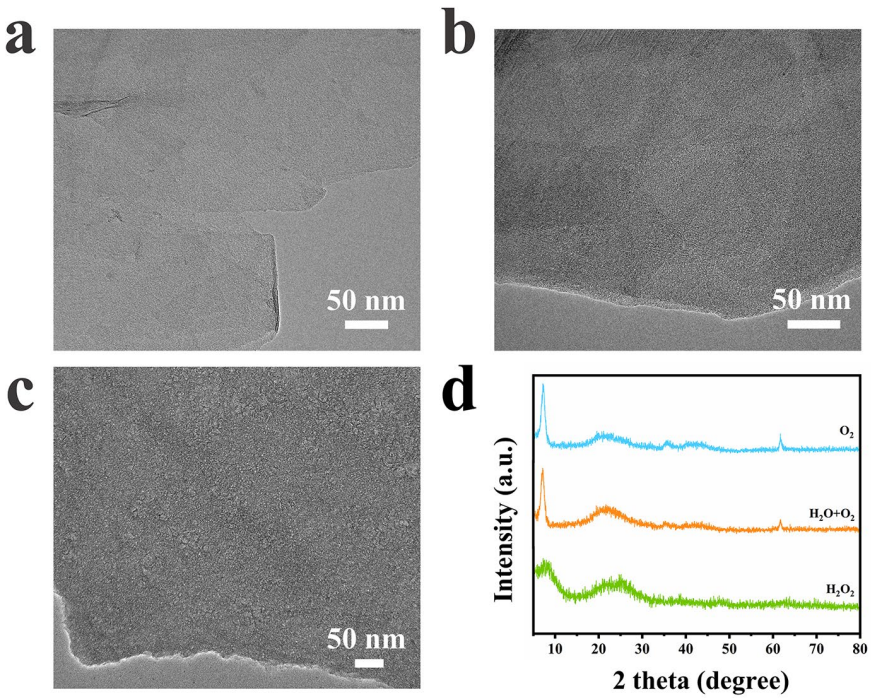

Fig. S27. The surface topographies and XRD patterns of MXene under three environments. TEM images of (a) individual MXene, (b) H_2O-treated MXene, and (c) H_2O_2-treated MXene. (d) Corresponding XRD patterns.

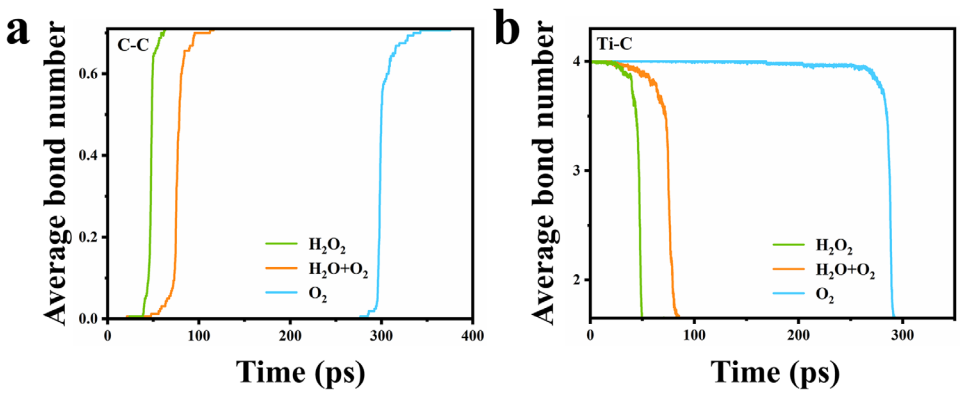

Fig. S28. Change of average bond number under dry air (O_2), wet air (H_2O+O_2), and H_2O_2 environmental conditions. (a) Average C-C bond number. (b) Average Ti-C bond number.

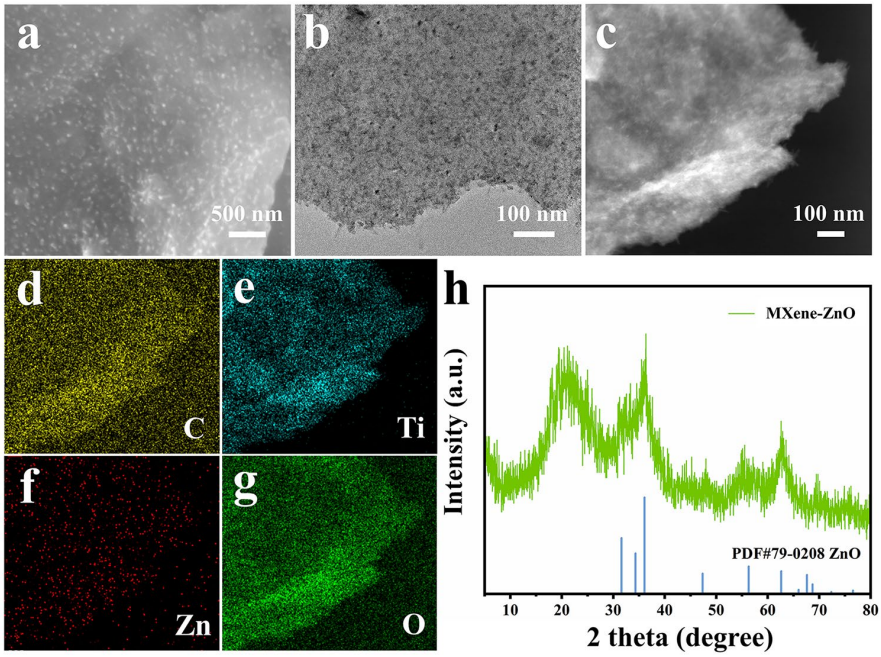

Fig. S29. The morphology and structure characterization of the MXene-ZnO. (a) SEM image. (b) TEM image. (c-g) HAADF-STEM image and the corresponding EDX maps of C, Ti, Zn, and O, showing the uniform distribution of elements. (h) XRD pattern which corresponds to ZnO phase.

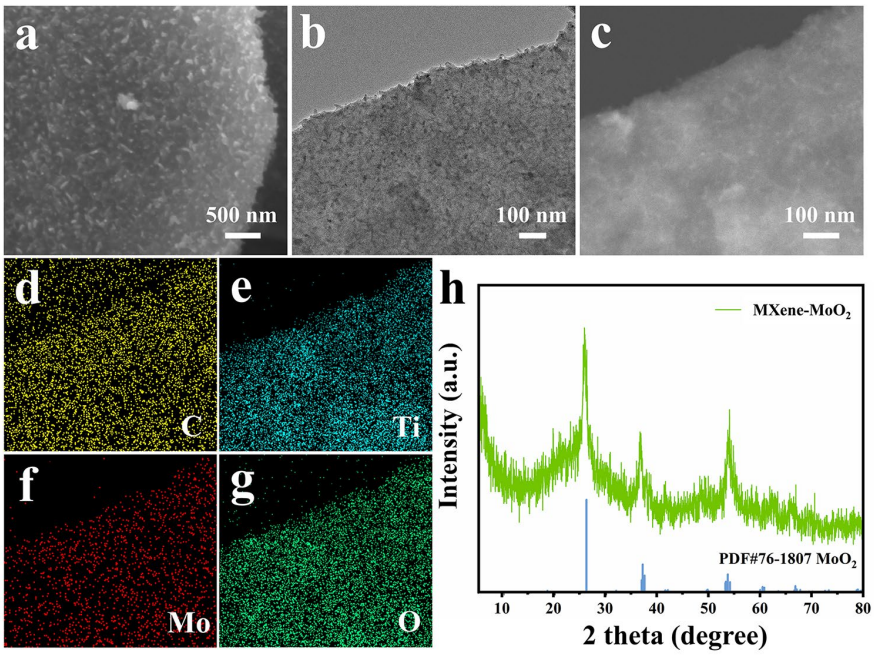

Fig. S30. The morphology and structure characterization of the MXene-MoO_2. (a) SEM image. (b) TEM image. (c-g) HAADF-STEM image and the corresponding EDX maps of C, Ti, Mo, and O, exhibiting homogeneous distribution of elements. (h) XRD pattern which corresponds to MoO_2 phase.

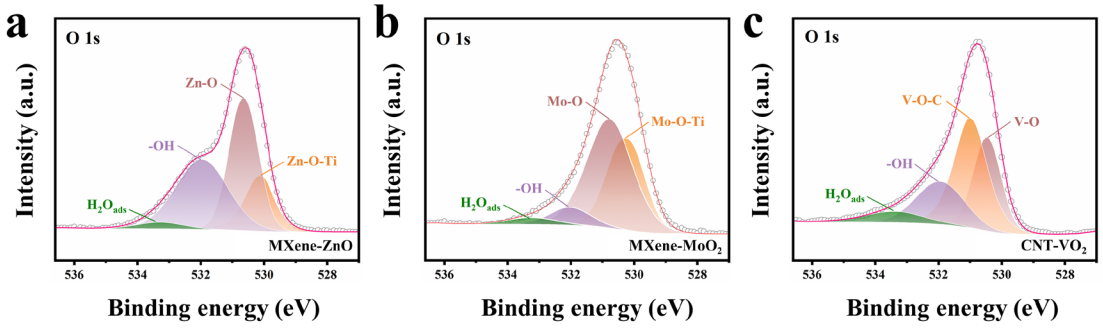

Fig. S31. O 1s spectra of (a) MXene-ZnO, (b) MXene-MoO_2, and (c) CNT-VO_2.

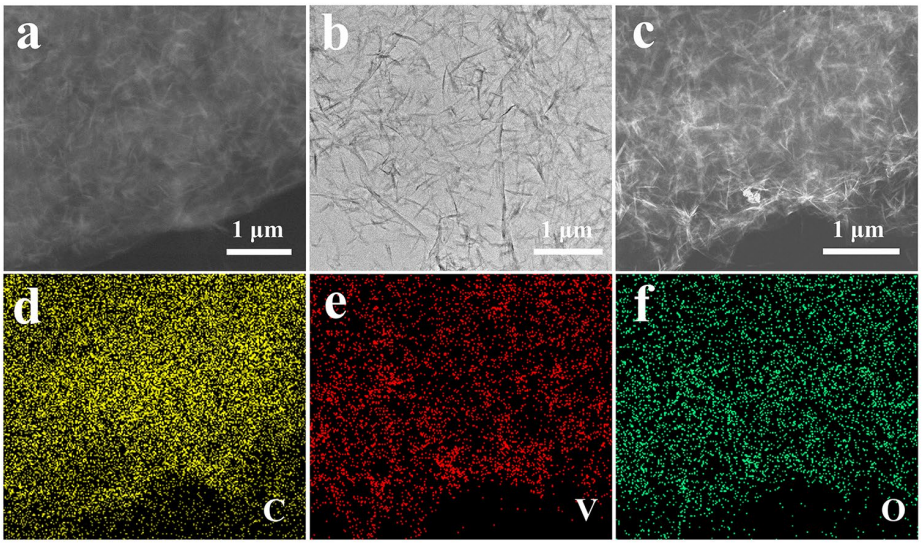

Fig. S32. The morphology characterization of the GO-VO_2. (a) SEM image. (b) TEM image. (c-f) HAADF-STEM image and the homogeneous EDX maps of C, V, and O.

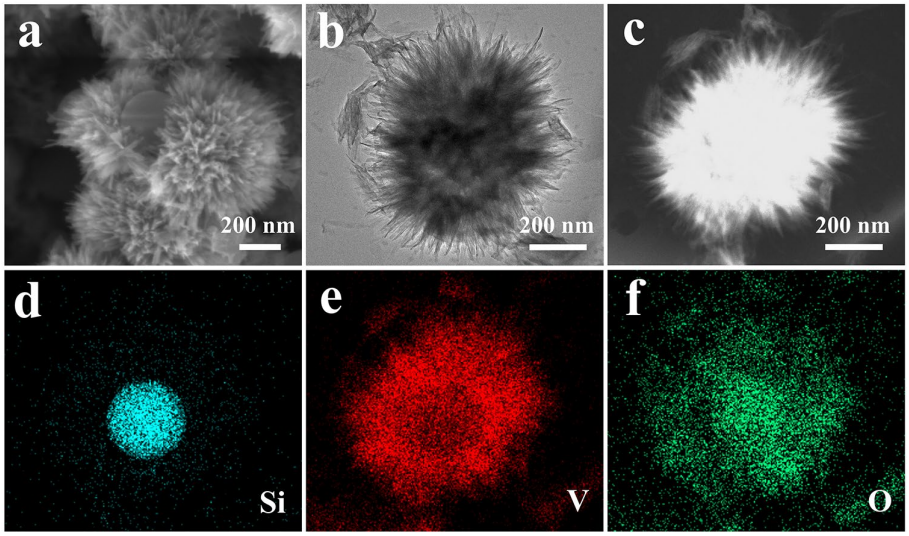

Fig. S33. The morphology characterization of the SiO_2-VO_2. (a) SEM image. (b) TEM image. (c-f) HAADF-STEM image and the distinguishing EDX maps of Si, V, and O.

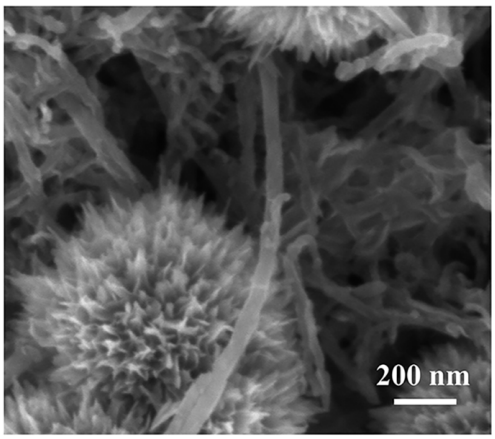

Fig. S34. SEM image of the phase separation between CNT and VO_2.

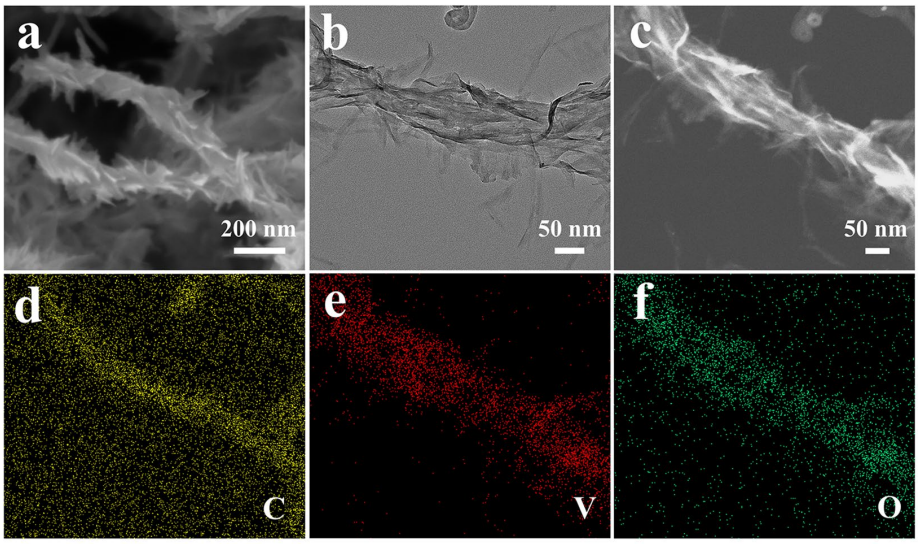

Fig. S35. The morphology characterization of the CNT-VO_2. (a) SEM image. (b) TEM image. (c-f) HAADF-STEM image and the distinguishing EDX maps of C, V, and O.

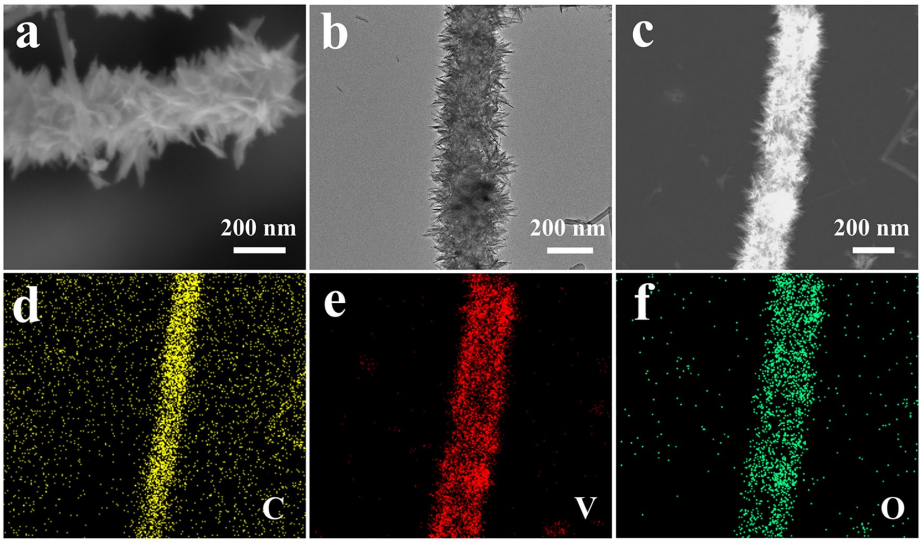

Fig. S36. The morphology characterization of the CF-VO_2. (a) SEM image. (b) TEM image. (c-f) HAADF-STEM image and the distinguishing EDX maps of C, V, and O.

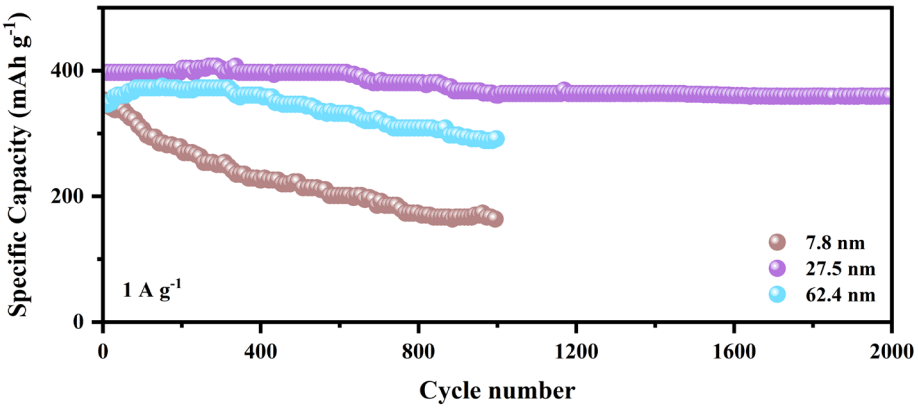

Fig. S37. The long-term cycle test of the MXene-VO_{2-x} cathode with different thickness at 1 A g^{-1}.

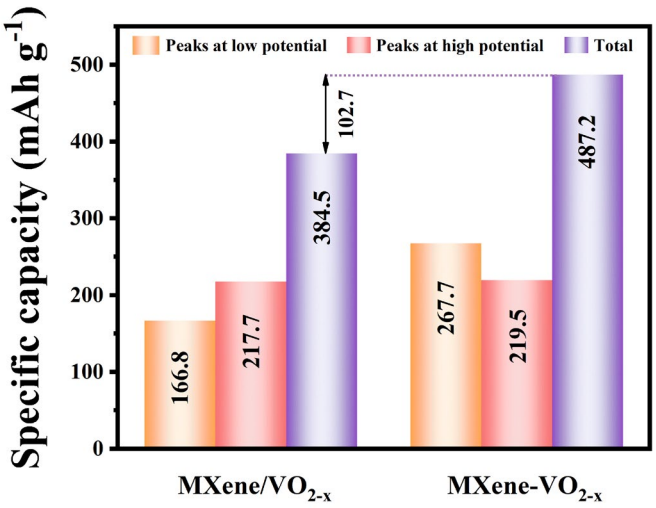

Fig. S38. The comparative distribution histogram of capacity contribution.

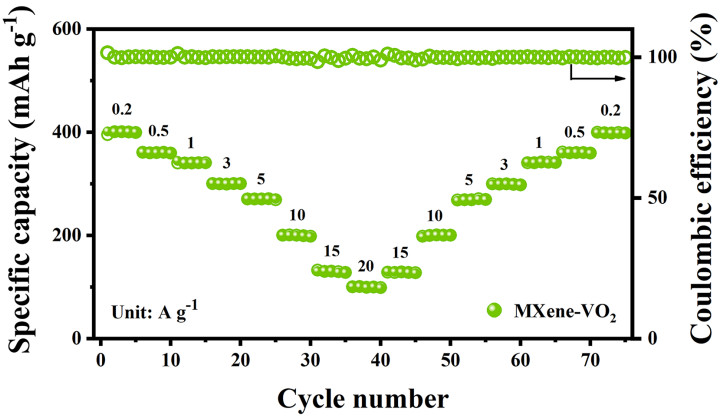

Fig. S39. Rate performance of the MXene-VO_2 cathode.

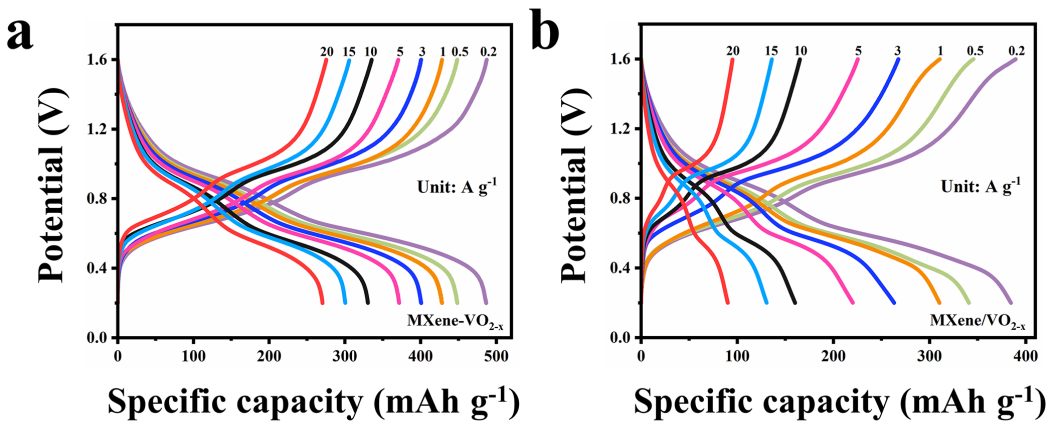

Fig. S40. The charge/discharge curves under different electrical current density. (a) MXene-VO_{2-x}. (b) MXene/VO_{2-x}.

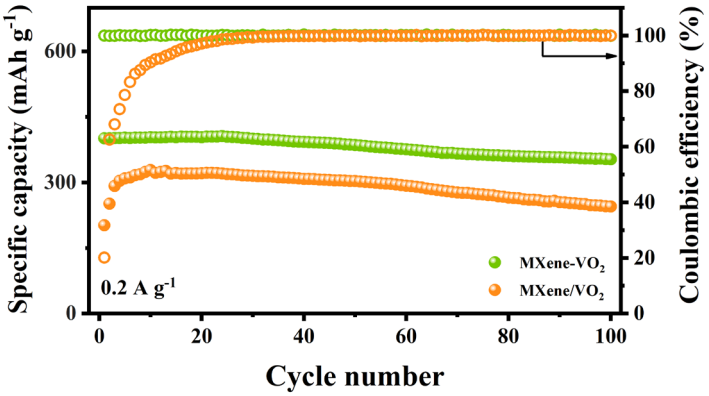

Fig. S41. Cycling performance of the MXene-VO_2 and MXene/VO_2 cathodes at 0.2 A g^{-1}.

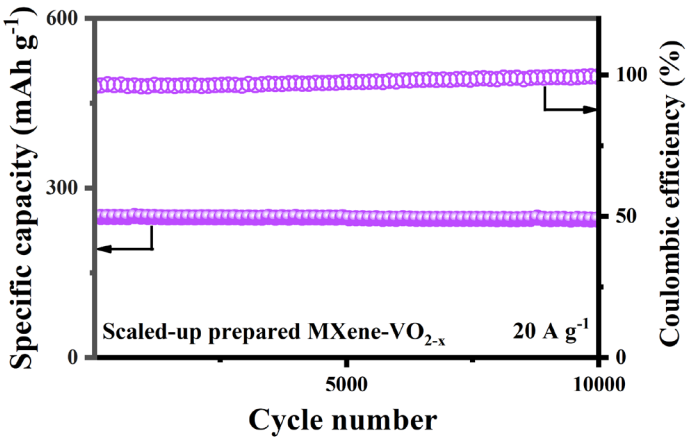

Fig. S42. Long-term cycle test at 20 A g^{-1} of the scaled-up prepared MXene-VO_{2-x} cathode.

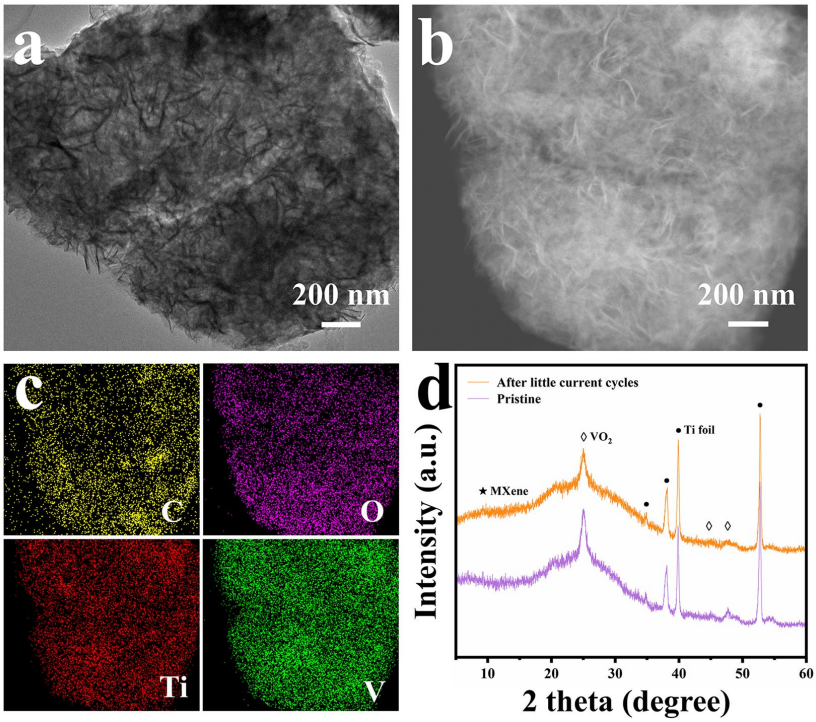

Fig. S43. The morphology characterization of the MXene-VO_{2-x} cathode after 100 cycles at 0.2 A g^{-1}. (a) TEM image. (b-c) HAADF-STEM image and the corresponding EDX maps of C, O, Ti and V. (d) XRD pattern.

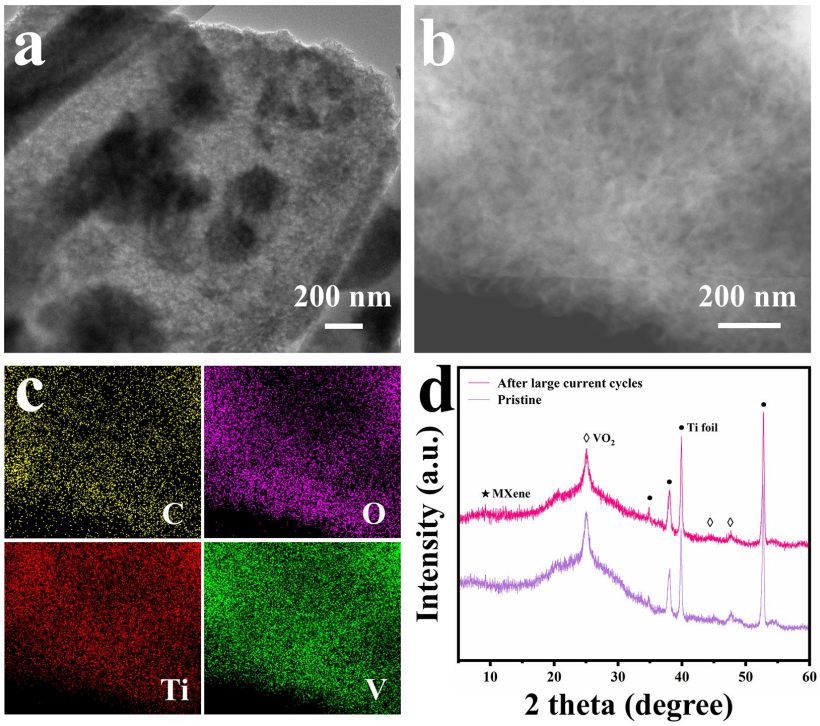

Fig. S44. The morphology characterization of the MXene-VO_{2-x} cathode after 30000 cycles at 20 A g^{-1}. (a) TEM image. (b-c) HAADF-STEM image and the corresponding EDX maps of C, O, Ti and V. (d) XRD pattern.

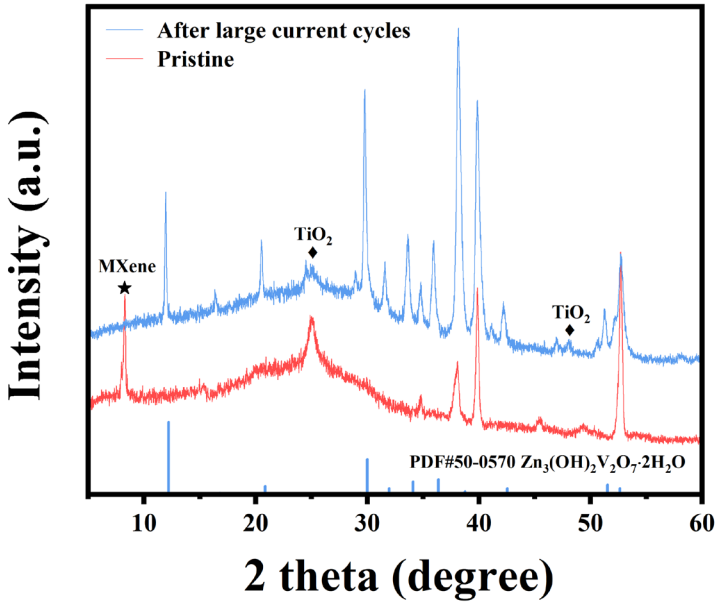

Fig. S45. The XRD pattern of MXene/VO_{2-x} cathode after 30000 cycles at 20 A g^{-1}.

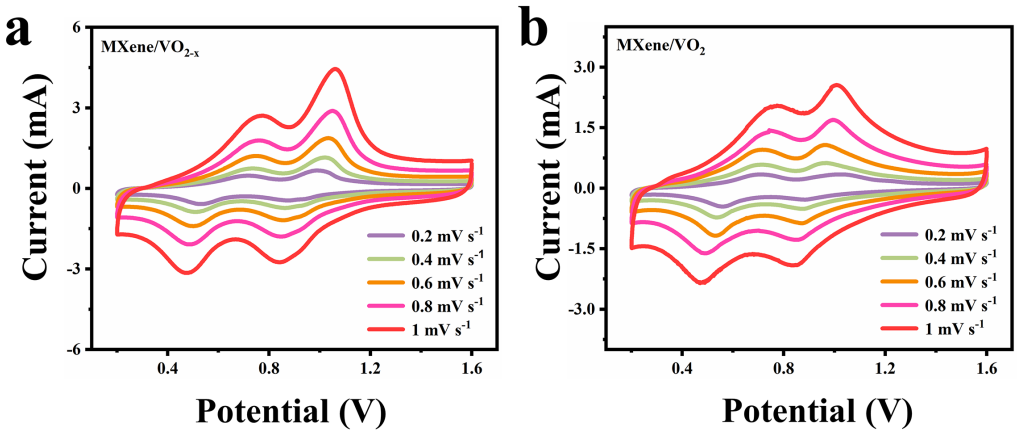

Fig. S46. CV curves for MXene/VO_{2-x} and MXene/VO_2 at different scan rates.

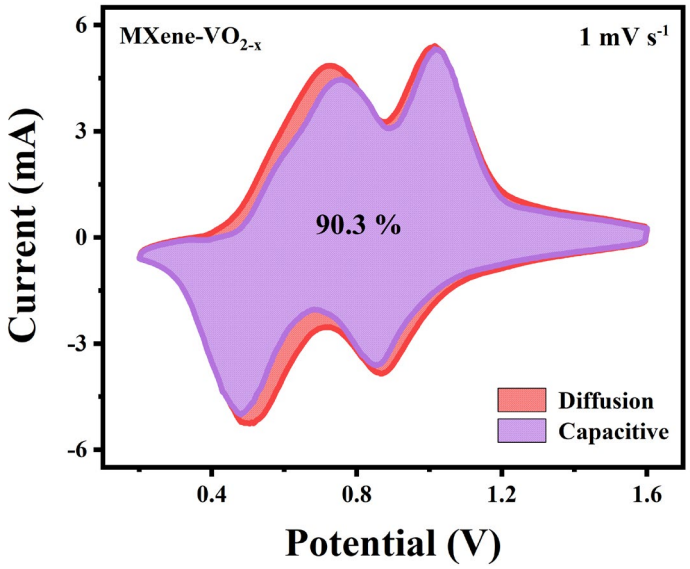

Fig. S47. CV curves of MXene-VO_{2-x} cathode with a capacitive contribution at 1.0 mV s^{-1}.

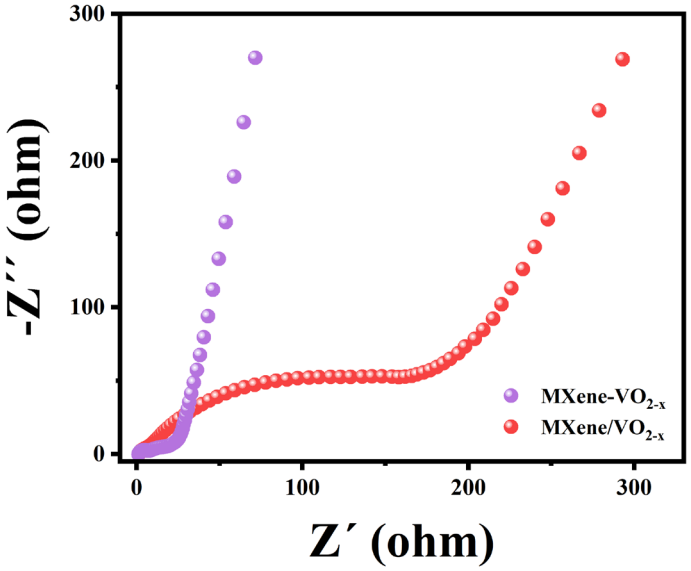

Fig. S48. Nyquist plots of MXene-VO_{2-x} and MXene/VO_{2-x} cathode.

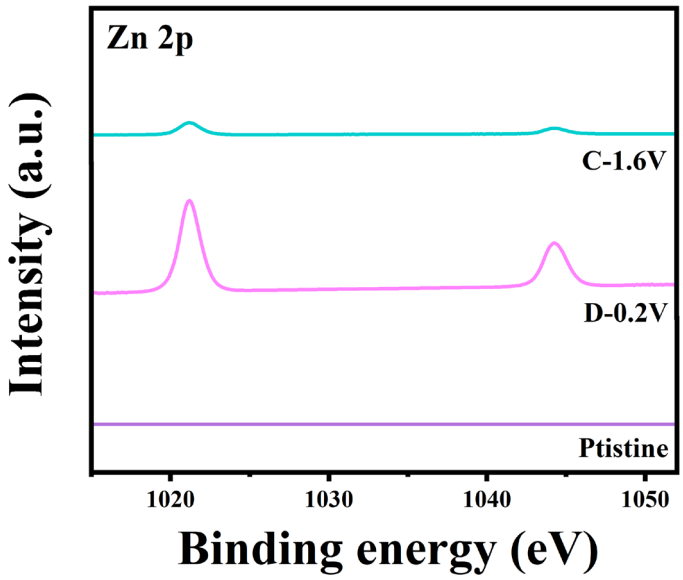

Fig. S49. Zn 2p spectra of MXene-VO_{2-x} after discharging and charging.

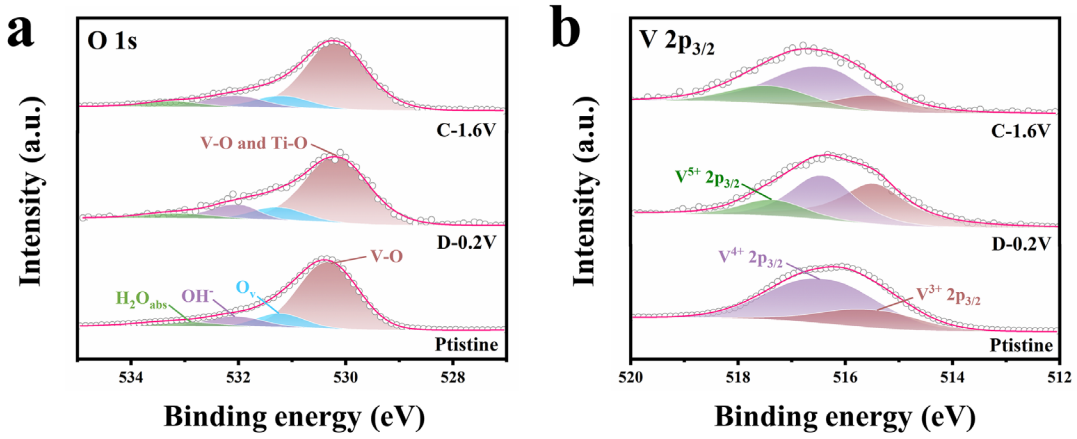

Fig. S50. The O 1s spectra and V $2p_{3/2}$ spectra of MXene/VO_{2-x} after discharging and charging.

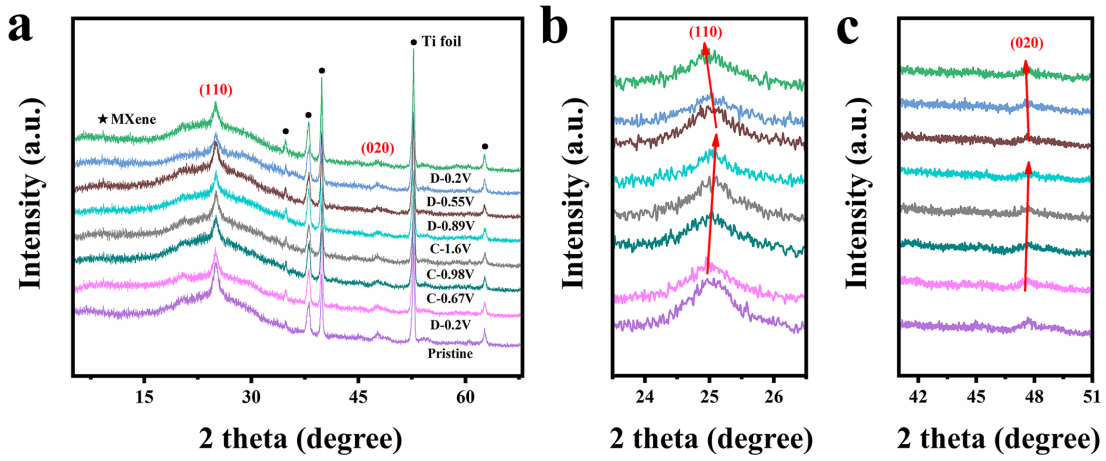

Fig. S51. (a) Ex situ XRD patterns of the MXene-VO_{2-x} cathode after discharging and charging. The peak appeared around 20.4 ° is attributed to the PVDF. (b) Magnified view of the (110) peaks. (c) Magnified view of the (020) peaks.

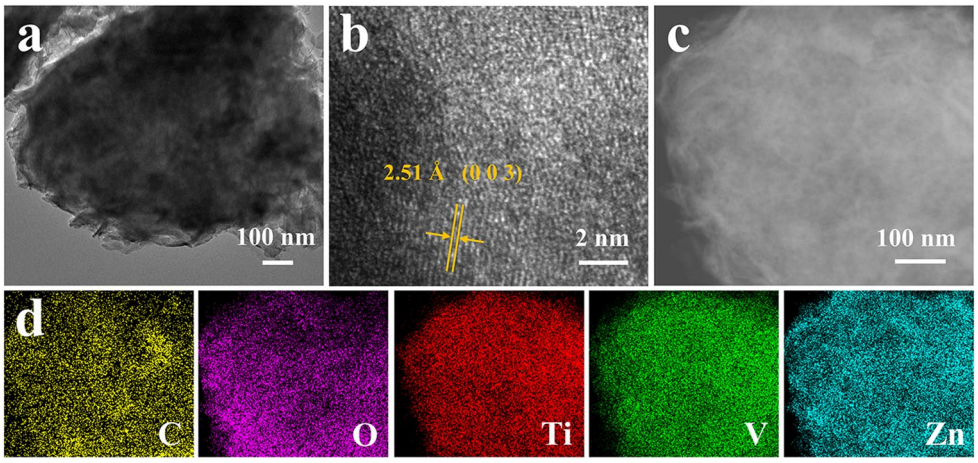

Fig. S52. The morphology characterization of the MXene-VO_{2-x} cathode after discharging to 0.2 V. (a) TEM image. (b) High resolution TEM image. The enlarged lattice spacing of 2.51 Å is attributed to the insertion of Zn^{2+}. (c) HAADF-STEM image. (d) The corresponding EDX maps of C, O, Ti, V and Zn.

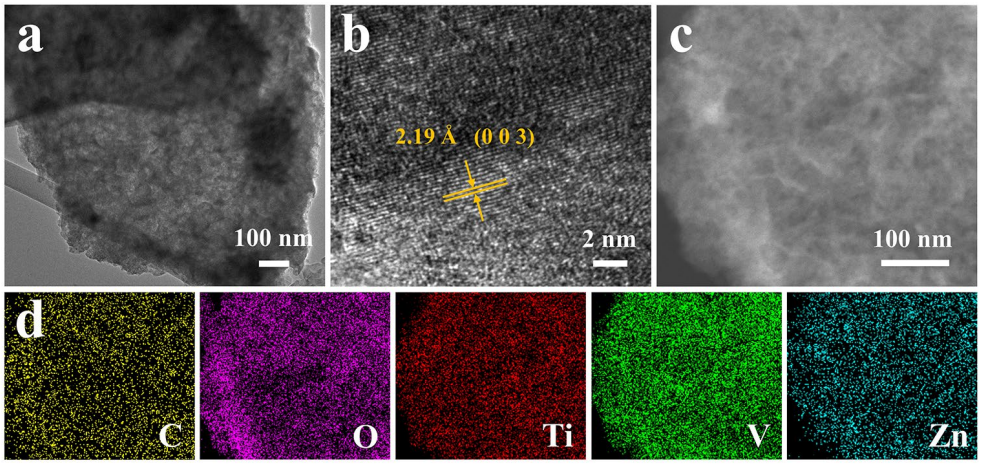

Fig. S53. The morphology characterization of the MXene-VO_{2-x} cathode after charging to 1.6 V. (a) TEM image. (b) High resolution TEM image. The observed lattice spacing of 2.19 Å corresponds to the (003) crystal plane of VO_2 (B). (c) HAADF-STEM image. (d) The corresponding EDX maps of C, O, Ti, V and Zn. The weak Zn signals in the sample should be due to the residual Zn^{2+} in the cathode.

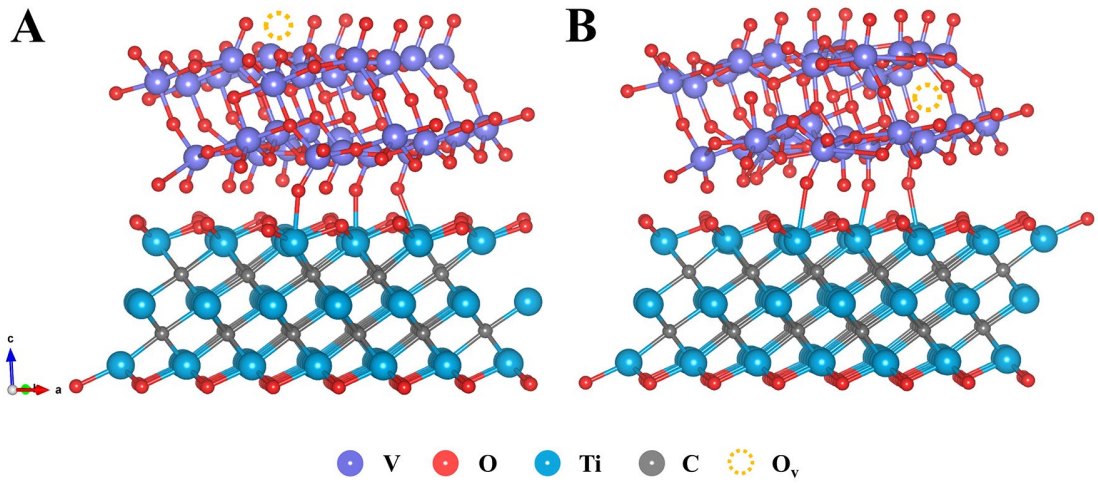

Fig. S54. DFT calculation models for the O_v configuration at (a) the apical sites and (b) the equatorial sites.

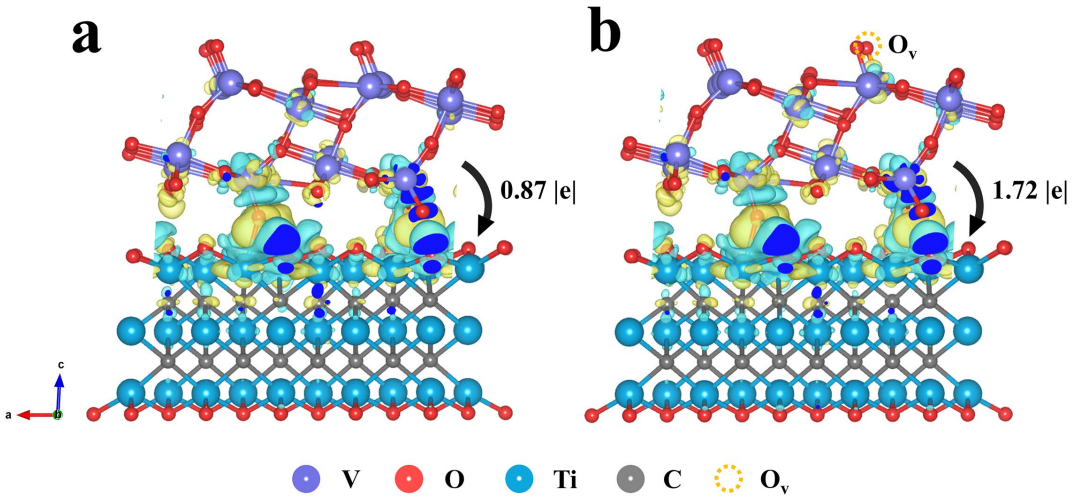

Fig. S55. The charge differential density models of MXene-VO_2 and MXene-VO_{2-x}. (Blue and yellow colors represent the loss and accumulation of electron, respectively.)

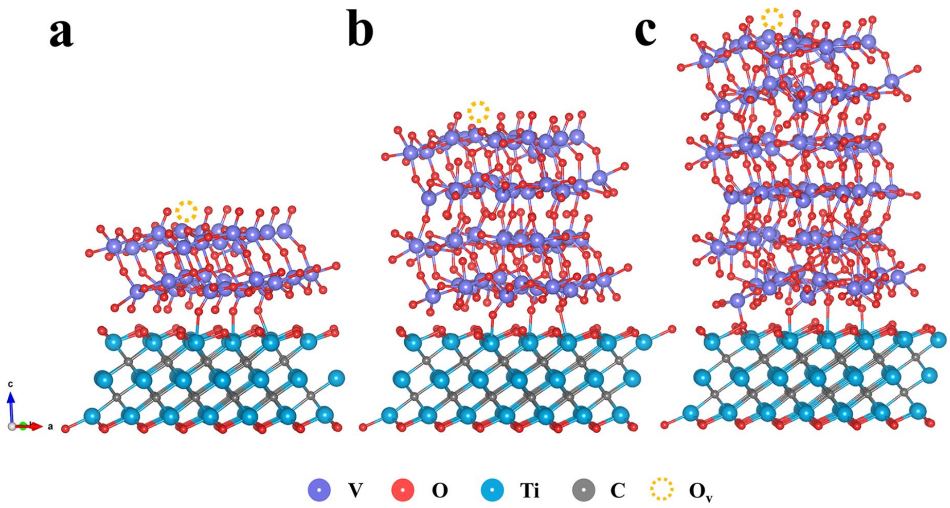

Fig. S56. DFT calculation models for different VO_2 layers configurations on MXene nanosheets with interfacial covalent bonding. (a) One layer. (b) Two layers. (c) Three layers.

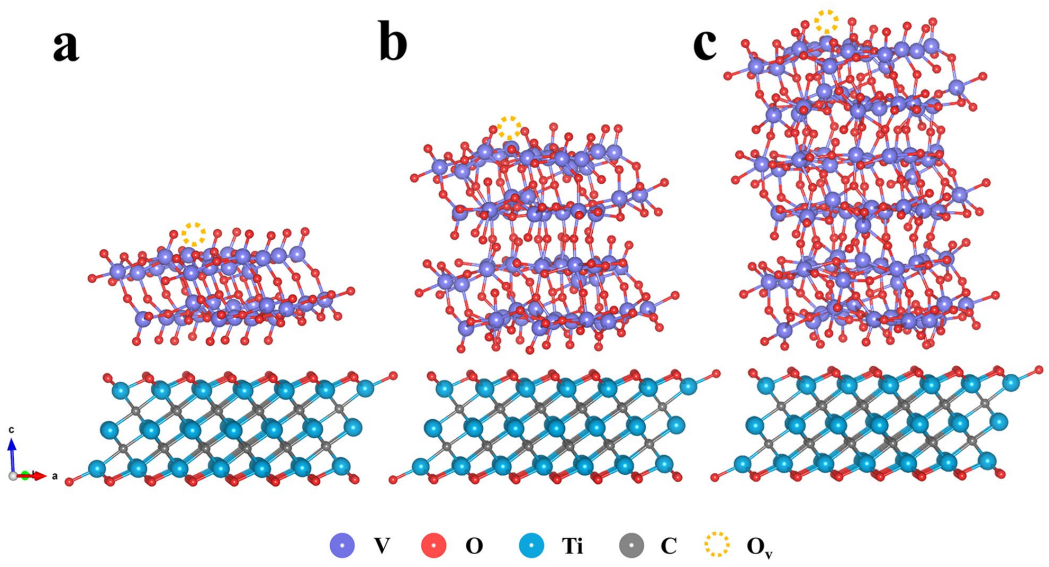

Fig. S57. DFT calculation models for different VO_2 layers configurations on MXene nanosheets without interfacial covalent bonding. (a) One layer. (b) Two layers. (c) Three layers.

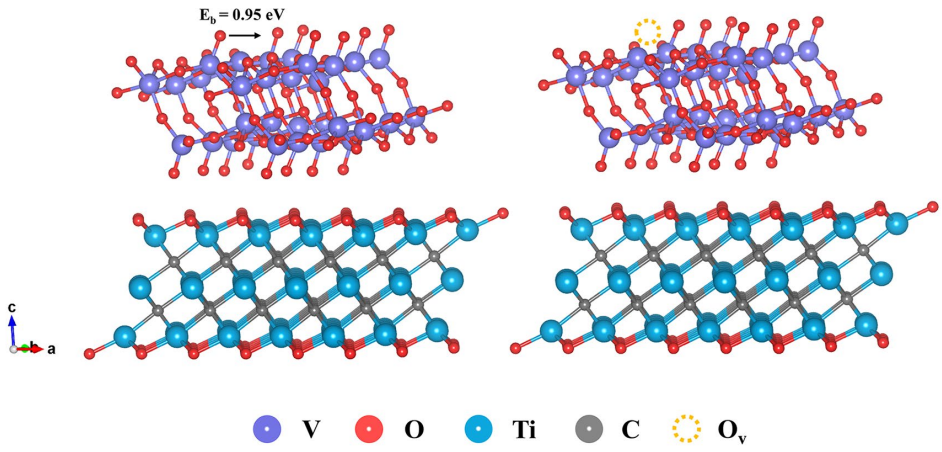

Fig. S58. Calculated models for the migration of oxygen atoms to neighboring sites on the MXene/VO_{2-x} in the absence of intercalated Zn^{2+}. The E_b of O_v was calculated to be 0.95 eV.

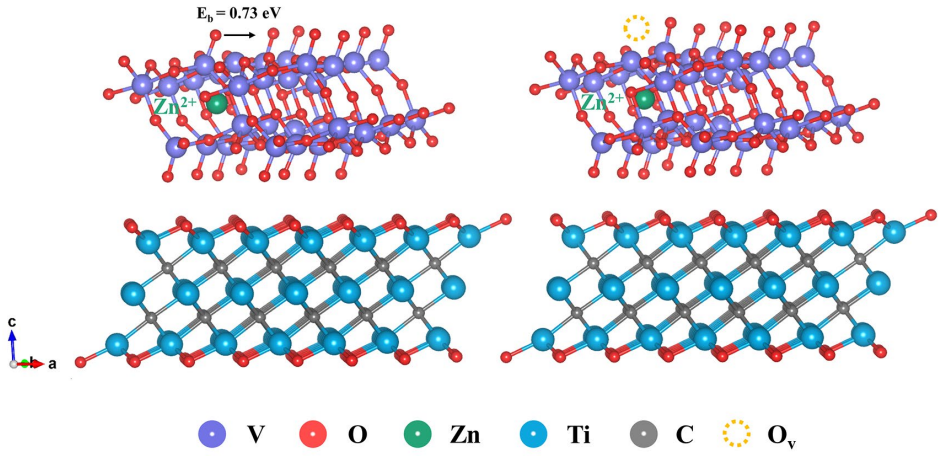

Fig. S59. Calculated models for the migration of oxygen atoms to neighboring sites on the MXene/VO_{2-x} in the presence of intercalated Zn^{2+}. The E_b of O_v was calculated to be 0.73 eV.

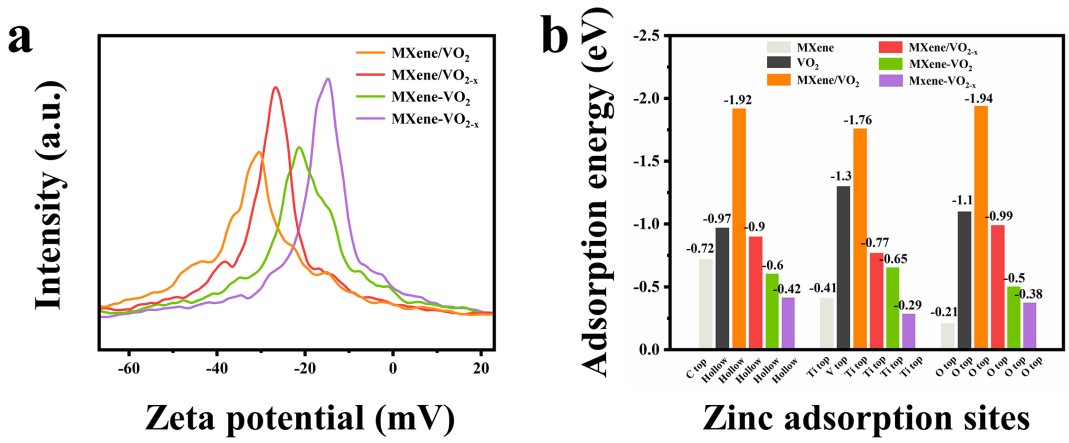

Fig. S60. Analysis for the adsorption behavior of Zn^{2+}. (a) Zeta potential measurements. (b) Adsorption energy of Zn^{2+} at different sites on the surfaces of MXene, VO_2, MXene/VO_2, MXene/VO_{2-x}, MXene-VO_2, and MXene-VO_{2-x}.

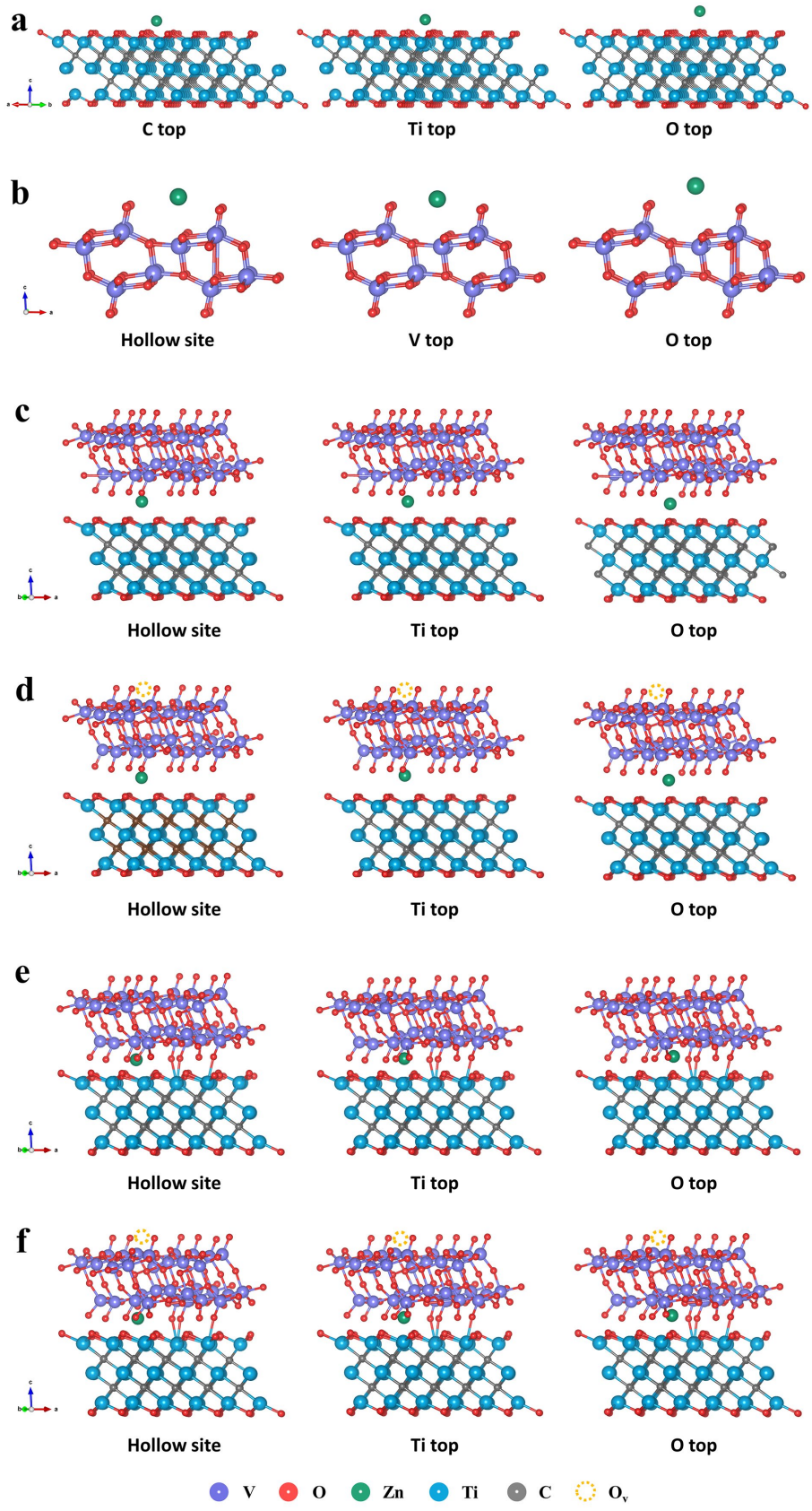

Fig. S61. Zn^{2+} adsorption models at different sites. (a) Zinc adsorption in MXene model at C top, Ti top and O top. (b) Zinc adsorption in VO_2 model at the hollow site, V top

and O top. (c) Zinc adsorption in the MXene/VO_2 heterointerface at the hollow site, Ti top and O top. (d) Zinc adsorption in the MXene/VO_{2-x} heterointerface at the hollow site, Ti top and O top. (e) Zinc adsorption in the MXene-VO_2 heterointerface at the hollow site, Ti top and O top. (f) Zinc adsorption in the MXene-VO_{2-x} heterointerface at the hollow site, Ti top and O top.

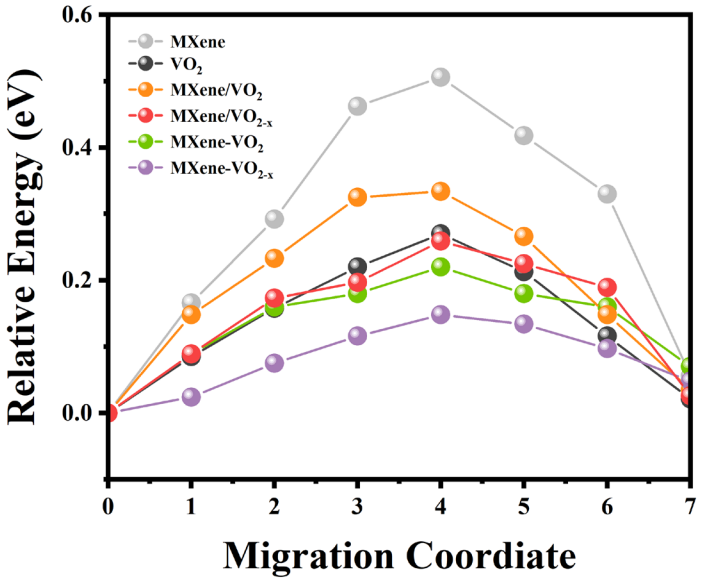

Fig. S62. Zinc diffusion energy barrier profiles of MXene, VO_2, MXene/VO_2, MXene/VO_{2-x}, MXene-VO_2, and MXene-VO_{2-x}.

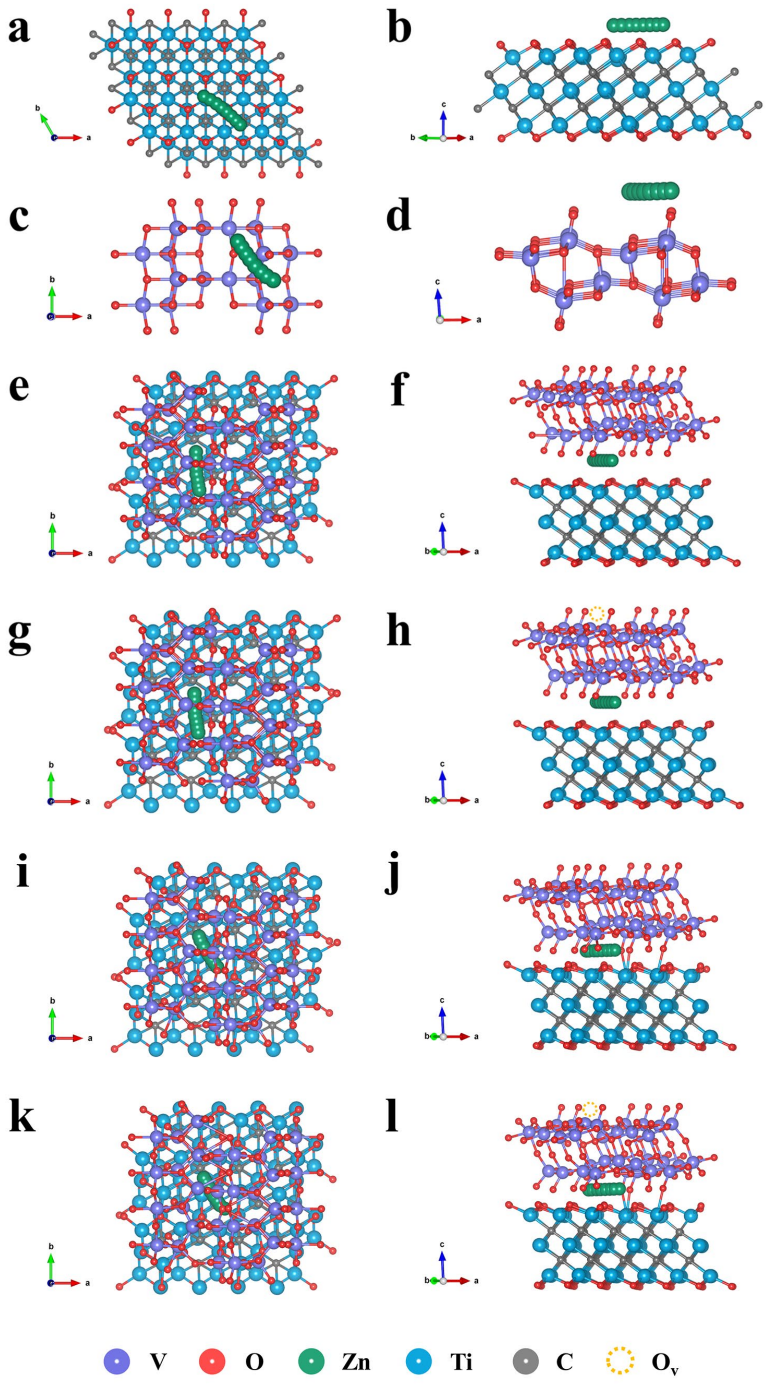

Fig. S63. The top and side view of Zn^{2+} migration pathways in different models. (a, b) MXene. (c, d) VO_2. (e, f) MXene/VO_2. (g, h) MXene/VO_{2-x}. (i, j) MXene-VO_2. (k, l) MXene-VO_{2-x}.

Supporting Tables

Supporting Table 1 Curvefit Parameters for V K-edge EXAFS for MXene-VO_2 and MXene-VO_{2-x}.

Sample	Path	S_0^2	N	ΔE_0	R / Å	σ^2 / 10^{-3} Å^2	R factor
MXene -VO_2	V-O1	0.8 ± 0.2	1.9	1.8 ± 2.3	1.64 ± 0.02	8 ± 2	0.7 %
	V-O2		2.4		1.93 ± 0.02	5 ± 2	
	V-O3		1.7		2.35 ± 0.02	8 ± 2	
	V-V		1		3.03 ± 0.03	9 ± 4	
MXene -VO_{2-x}	V-O1	0.8	1.3	3.4 ± 1.8	1.63 ± 0.01	5 ± 1	1.6 %
	V-O2		2.5 ± 0.2		1.94 ± 0.01	5 ± 1	
	V-O3		0.9		2.39 ± 0.03	6 ± 4	
	V-V		1.1 ± 0.7		3.05 ± 0.03	9 ± 7	

The coordination numbers of MXene-VO_2 are fixed as the nominal values. The obtained S_0^2 is fixed in the subsequent fitting of MXene-VO_{2-x}. While the internal atomic distances R, Debye-Waller factor σ^2, and the edge-energy shift ΔE_0 are refined as global fit parameters. Data ranges: $2.0 < k < 13.0$ Å, $1.0 < R < 3.0$ Å. All the distances are from the crystal structure of VO_2 (B).

Supporting Table 2 Electrochemical performances of recently reported vanadium oxide-based cathode materials of AZIBs.

Cathode	Electrolyte	Voltage window	Specific capacity/ Rate performance	Cycling performance	Ref
MXene-VO_{2-x}	2M $Zn(CF_3SO_3)_2$	0.2-1.6V	487.2 mAh g^{-1} at 0.2 A g^{-1} 270.5 mAh g^{-1} at 20 A g^{-1}	266.6 mAh g^{-1} retained (98.6 %) after 30000 cycles at 20 A g^{-1}	This work
Phenylamine-intercalated $VOPO_4 \cdot 2H_2O$	2M $Zn(CF_3SO_3)_2$	0.2-1.9V	268.2 mAh g^{-1} at 0.1 A g^{-1} 187.5 mAh g^{-1} at 10 A g^{-1}	200 mAh g^{-1} (92.3 %) retained after 2000 cycles at 5 A g^{-1}	12
C_3N_4 pillared $NH_4V_4O_{10}$	3M $Zn(CF_3SO_3)_2$	0.2-1.6V	364.3 mAh g^{-1} at 0.5 A g^{-1} 289.3 mAh g^{-1} at 10 A g^{-1}	219.9 mAh g^{-1} (76 %) retained after 10000 cycles at 10 A g^{-1}	13
Amorphous-crystalline VO_x	10 M $ZnCl_2$	0.2-1.9V	516 mAh g^{-1} at 0.5 A g^{-1} 316 mAh g^{-1} at 20 A g^{-1}	85.5 % retained after 5000 cycles at 20 A g^{-1}	14
O_d-V_6O_{13}	3M $Zn(CF_3SO_3)_2$	0.2-1.5V	410 mAh g^{-1} at 0.2 A g^{-1} 223 mAh g^{-1} at 5 A g^{-1}	253.1 mAh g^{-1} retained (86 %) after 2000 cycles at 2 A g^{-1}	15
V_d-V_2O_3	3M $Zn(CF_3SO_3)_2$	0.1-1.3V	196 mAh g^{-1} at 0.1 A g^{-1} 113 mAh g^{-1} at 4 A g^{-1}	95 mAh g^{-1} (81 %) retained after 30000	16

				cycles at 5 A g^{-1}	
O_d-VO_2·H_2O	3 M $ZnSO_4$	0.4-1.4V	396 mAh g^{-1} at 0.05 A g^{-1} 88 mAh g^{-1} at 50 A g^{-1}	140 mAh g^{-1} retained after 1000 cycles at 10 A g^{-1}	17
Amorphous V_2O_5/GO	3 M $ZnSO_4$	0.2-1.8V	489 mAh g^{-1} at 0.1 A g^{-1} 123 mAh g^{-1} at 70 A g^{-1}	240 mAh g^{-1} retained (87 %) after 3000 cycles at 30 A g^{-1}	18
VO_x/rGO	3M $Zn(CF_3SO_3)_2$	0.3-1.5V	443 mAh g^{-1} at 0.1 A g^{-1} 158 mAh g^{-1} at 100 A g^{-1}	283 mAh g^{-1} retained after 1000 cycles at 20 A g^{-1}	19
V_5O_{12-x}·$6H_2O$@ $CaSO_4$·$2H_2O$	2M $Zn(CF_3SO_3)_2$ +0.1 M $ZnSO_4$	0.4-1.6V	402.5 mAh g^{-1} at 0.2 A g^{-1} 225.5 mAh g^{-1} at 10 A g^{-1}	231.6 mAh g^{-1} (75.4 %) retained after 4000 cycles at 3 A g^{-1}	20
CNT/VOOH	3M $Zn(CF_3SO_3)_2$	0.2-1.8V	533 mAh g^{-1} at 0.1 A g^{-1} 322 mAh g^{-1} at 20 A g^{-1}	206 mAh g^{-1} retained after 8500 cycles at 10 A g^{-1}	21
Dispersive VO_2 (B)	3M $Zn(CF_3SO_3)_2$	0.2-1.5V	420.8 mAh g^{-1} at 0.1 A g^{-1} 344.8 mAh g^{-1} at 10 A g^{-1}	279.5 mAh g^{-1} (84.3 %) retained after 5000 cycles at 10 A g^{-1}	22

References

1 G. Kresse and J. Hafner, *Phys. Rev. B*, 1993, **47**, 558−561.

2 P. E. Blöchl, *Phys. Rev. B*, 1994, **50**, 17953−17979.

3 G. Kresse and D. Joubert, *Phys. Rev. B*, 1999, **59**, 1758−1775.

4 S. Grimme, *J. Comput. Chem.*, 2006, **27**, 1787−1799.

5 G. Henkelman, B. P. Uberuaga and H. Jonsson, *J. Chem. Phys.*, 2000, **113**, 9901−9904.

6 S. Plimpton, *J. Comput. Phys.*, 1995, **117**, 1−19.

7 A. C. T. Van Duin, S. Dasgupta, F. Lorant and W. A. Goddard, *J. Phys. Chem. A*, 2001, **105**, 9396−9409.

8 Y. Q. Fu, J. Y. Wu, S. B. Xiao, S. Q. Liu, Z. L. Zhang and J. Y. He, *Carbon*, 2021, **184**, 146−155.

9 H. Z. Yu, K. Xu, Z. S. Zhang, X. Z. Cao, J. Weng and J. Y. Wu, *J. Mater. Chem. C*, 2021, **9**, 2416−2425.

10 R. Fu, Y. H. Xu, S. Qiao, Y. S. Liu, Y. W. Lin, Y. Li, Z. S. Zhang and J. Y. Wu, *J. Phys.: Condens. Matter.*, 2022, **34**, 425402.

11 C. Sui, Y. S. Zhao, Z. S. Zhang, J. Y. He, Z. L. Zhang, X. D. He, C. Wang and J. Y. Wu, *ACS Omega*, 2017, **2**, 3977−3988.

12 L. F. Hu, Z. Y. Wu, C. J. Lu, F. Ye, Q. Liu and Z. M. Sun, *Energy Environ. Sci.*, 2021, **14**, 4095−4106.

13 Y. Xu, G. L. Fan, P. X. Sun, Y. Guo, Y. Y. Wang, X. J. Gu, L. M. Wu and L. Yu, *Angew. Chem. Int. Ed.*, 2023, **62**, e202303529.

14 Z. H. Wang, Y. Song, J. Wang, Y. L. Lin, J. M. Meng, W. B. Cui and X. -X. Liu, *Angew. Chem. Int. Ed.*, 2023, **62**, e202216290.

15 M. Liao, J. W. Wang, L. Ye, H. Sun, Y. Z. Wen, C. Wang, X. M. Sun, B. J. Wang and H. S. Peng, *Angew. Chem. Int. Ed.*, 2020, **59**, 2273−2278.

16 K. F. Zhu, S. Q. Wei, H. W. Shou, F. R. Shen, S. M. Chen, P. J. Zhang, C. D. Wang, Y. Y. Cao, X. Guo, M. Luo, H. J. Zhang, B. J. Ye, X. J. Wu, L. H. He and L. Song, *Nat. Commun.*, 2021, **12**, 6878.

17 N. N. Liu, X. Wu, L. S. Fan, S. Gong, Z. K. Guo, A. S. Chen, C. Y. Zhao, Y. C. Mao, N. Q. Zhang and K. N. Sun, *Adv. Mater.*, 2020, **32**, 1908420.

18 X. Wang, Y. G. Li, S. Wang, F. Zhou, P. Das, C. L. Sun, S. H. Zheng and Z. -S. Wu, *Adv. Energy Mater*., 2020, **10**, 2000081.

19 Y. H. Dai, X. B. Liao, R. H. Yu, J. H. Li, J. T. Li, S. S. Tan, P. He, Q. Y. An, Q. L. Wei, L. N. Chen, X. F. Hong, K. N. Zhao, Y. Ren, J. S. Wu, Y. Zhao and L. Q. Mai, *Adv. Mater.*, 2021, **33**, 2100359.

20 J. T. Huang, H. P. Liang, Y. Tang, B. G. Lu, J. Zhou and S. Q. Lian, *Adv. Energy Mater*., 2022, **12**, 2201434.

21 X. L. Shi, Y. C. Sun, Y. B. Weng, X. Y. Long, T. X. Lei, J. L. Zhou, D. P. Li, J. Zhang, Y. Huang, L. J. Ci, K. K. Li and T. -Y. Zhang, *Energy Environ. Sci*., 2023, **16**, 4670−4678.

22 Q. He, T. Hu, Q. Wu, C. Wang, X. R. Han, Z. B. Chen, Y. W. Zhu, J. Y. Chen, Y. Zhang, L. Shi, X. B. Wang, Y. W. Ma and J. Zhao, *Adv. Mater.*, 2024, **36**, 2400888.